



Metabolomics and proteomics reveal blocking argininosuccinate synthetase 1 alleviates colitis in mice

Received: 2 September 2024

Accepted: 16 July 2025

Published online: 30 July 2025

Check for updates

Shijia Liu^{1,14}✉, Haijian Sun^{②,14}✉, Zijing Du^{3,4,14}, Shuai Lu^③, Chenwen Wang⁶, Ye Zhang⁶, Zichen Luo⁷, Lu Wang⁸, Zhimin Fan⁸, Peng Wei¹, Yujiao Yan⁹, Junzhi Zhang¹, Shusheng Yin⁹, Tongtong Liu¹, Qiongzi He¹, Xi Guo⁶, Kang Ding⁸, Jingjie Zhou¹⁰, Haibing Hua¹⁰, Chengli Yu¹¹, Weichen Xu⁷, Jinjun Shan^{③,7}, Yongming Li⁹, Yi Xu¹, Xiaotao Shen^{③,12}✉, Gang Cao^{③,13}✉ & Wei Zhou^{③,6}✉

To date, treating ulcerative colitis (UC) remains a significant challenge due to its complex etiology. In this study, metabolomics and proteomics analysis for multi-center cohorts reveal that both serum arginine levels and the rate-limiting enzyme argininosuccinate synthetase 1 (ASS1) are significantly elevated in UC patients. Exogenous arginine infusion and ASS1 overexpression exacerbate the pathological features of colitis in mice, while inhibiting or silencing ASS1 offers protection against experimental colitis. The induction of ASS1 is accompanied by increased levels of acetylated H3 and trimethylated H3K4, along with decreased levels of dimethyl H3K9 around the ASS1 promoters, suggesting epigenetic activation of ASS1 in colitis. The ASS1/arginine axis triggers mTOR and iNOS activation and induces gut microbiota dysbiosis, leading to experimental colitis. Additionally, we identify a screened compound, C-01, which significantly improves colitis by highly binding to ASS1. Our findings suggest that ASS1 could be a promising target for UC treatment.

Ulcerative colitis (UC) is a chronic idiopathic inflammatory bowel disease (IBD) characterized by diffuse inflammation in the colonic mucosa, leading to recurrent episodes, diminished quality of life, and an increased risk of colitis-related colorectal cancer. UC has emerged

as a global health challenge, placing a substantial burden on patients and healthcare systems^{1,2}. According to the latest epidemiological survey, the prevalence of IBD among the total population exceeded 0.3% in Canada, Denmark, Germany, Hungary, Australia, New Zealand,

¹Affiliated Hospital of Nanjing University of Chinese Medicine, Jiangsu Province Hospital of Chinese Medicine, Nanjing, Jiangsu, China. ²Wuxi School of Medicine, Jiangnan University, Jiangsu, China. ³Singapore Phenome Center, Lee Kong Chian School of Medicine, Nanyang Technological University, Singapore, Singapore. ⁴Guangdong Eye Institute, Department of Ophthalmology, Guangdong Provincial People's Hospital (Guangdong Academy of Medical Sciences), Southern Medical University, Guangzhou, China. ⁵School of Science, China Pharmaceutical University, Nanjing, China. ⁶State Key Laboratory of Natural Medicines, School of Traditional Chinese Pharmacy, China Pharmaceutical University, Nanjing, China. ⁷Institute of Pediatrics, Jiangsu Key Laboratory of Pediatric Respiratory Disease, Medical Metabolomics Center, Nanjing University of Chinese Medicine, Nanjing, Jiangsu, China. ⁸Jiangsu Clinical Innovation Center for Anorectal Diseases of T.C.M., Nanjing Hospital of Chinese Medicine Affiliated to Nanjing University of Chinese Medicine, Nanjing, P.R. China. ⁹School of Medicine & Holistic Integrative Medicine, Nanjing University of Chinese Medicine, Nanjing, China. ¹⁰The Affiliated Jiangyin Hospital of Nanjing University of Chinese Medicine, Jiangyin, China. ¹¹Jiangsu Key Laboratory for Functional Substances of Chinese Medicine, School of Pharmacy, Nanjing University of Chinese Medicine, Nanjing, Jiangsu, China. ¹²School of Chemistry, Chemical Engineering and Biotechnology, Nanyang Technological University, Singapore, Singapore. ¹³School of Pharmacy, Zhejiang Chinese Medical University, Hangzhou, Zhejiang, China. ¹⁴These authors contributed equally: Shijia Liu, Haijian Sun, Zijing Du. ✉e-mail: liushijia2011@163.com; sunhaijian927@163.com; xiaotao.shen@ntu.edu.sg; caogang33@163.com; zhouwei19860506@163.com

Sweden, the United Kingdom, and the United States³. The development of UC is driven by a complex interplay of factors, including environmental exposures, genetic susceptibility, immune dysregulation, metabolic disturbances, gut microbiota imbalances, and unhealthy dietary patterns^{4–7}. Despite significant progress in understanding the pathogenesis of UC, the precise mechanisms underlying its pathogenesis remain incompletely understood. Current therapies, such as 5-aminosalicylic acid (5-ASA), corticosteroids, and biologics targeting tumor necrosis factor (TNF)- α , have improved disease management but are associated with several challenges, including suboptimal remission rates, diminished efficacy over time, high healthcare costs, and adverse side effects^{8–10}. These limitations underscore the urgent need to explore therapeutic strategies that target key aspects of UC pathophysiology.

Metabolomics, the systematic study of small molecules (metabolites) within biological systems, has emerged as a powerful tool to investigate the biochemical changes associated with disease pathogenesis¹¹. In recent years, researchers have increasingly focused on the disrupted metabolic pathways involved in the development and progression of UC¹². Specifically, dysfunctions in blood and faecal amino acid metabolism, urine purine metabolism, faecal bile acids metabolism, urine vitamin metabolism, and mucosal lipid metabolism have been closely linked to the pathogenesis of UC^{13–16}. Metabolomics analyses have shown that changes in faecal short-chain fatty acids are associated with the therapeutic outcomes of UC patients undergoing fecal microbiota transplantation¹⁷. Elevated plasma levels of isoleucine and valine may correlate with the severity of UC, while decreased levels of L-lysine, histidine, phenylalanine, and tyrosine indicate UC remission^{15,16}. In addition, levels of phosphatidylcholine, ceramide, and sphingomyelin are significantly altered in the mucosal tissues of UC patients¹⁴. These findings consistently suggest that metabolic disorders play a crucial role in UC pathogenesis. Microbial oxazoles induce intestinal inflammation by modulating natural killer T cell-dependent inflammation by regulating lipid antigen presentation by CD1d on intestinal epithelial cells¹⁸. Deoxycholic acid (DCA) exacerbates colonic inflammation by causing the accumulation of ferrous ions and ferroptosis in intestinal epithelial cells¹⁹. DCA dose-dependently promoted the differentiation of CD4 $^{+}$ T cells into the Th17 lineage with a pathogenic signature, and DCA treatment significantly increased intestinal Th17 cell infiltration and exacerbated TNBS-induced colitis²⁰. In mice and humans, intestinal inflammation severity negatively correlates with the amount of xanthurenic (XANA) and kynurenic (KYNA) acids. Supplementation with XANA or KYNA decreases colitis severity through effects on intestinal epithelial cells and T cells, involving Aryl hydrocarbon Receptor (AhR) activation and the rewiring of cellular energy metabolism²¹. Butyrate alleviated dextran sodium sulfate (DSS)-induced colitis by regulating autophagy via HIF-1 α in intestinal epithelial cells²². These findings highlight diverse mechanisms through which microbial metabolites, bile acids, and dietary compounds modulate intestinal inflammation and immune responses, offering potential therapeutic targets for colitis.

Despite these findings, significant gaps remain in identifying specific endogenous metabolites and the precise mechanisms through which they contribute to UC pathogenesis. Understanding these metabolic disruptions could reveal biomarkers for disease severity and therapeutic targets. In this study, we aim to address these gaps by systematically investigating key metabolic pathways and their contribution to the onset and progression of UC, providing insights into potential avenues for effective treatment strategies.

In this work, to investigate the potential link between metabolic profile alterations and the pathological processes of UC, we conduct a comprehensive comparison of the serum metabolic profiles of 131 UC patients and 127 age- and sex-matched healthy control participants using liquid chromatography-mass spectrometry (LC-MS)-based untargeted metabolomics. We identify 49 differential metabolites

between healthy controls and UC participants. Pathway enrichment analysis reveals that the mTOR signaling pathway was among the top-enriched pathways, where mTOR overactivation in the colonic epithelium is known to drive the onset of UC²³. In addition, we find that serum arginine levels were significantly upregulated in UC patients, with its levels showing the strongest positive correlation with the Mayo score. The elevated serum arginine levels in UC patients are further validated using targeted metabolomics across three independent human cohorts. Arginine, an amino acid that directly activates mTOR, a nutrient-sensing kinase strongly implicated in UC^{24,25}. Our findings also show that the rate-limiting enzyme in arginine biosynthesis, argininosuccinate synthetase 1 (ASS1), is significantly upregulated in the colonic tissues of UC patients, as confirmed by proteomics, immunoblotting, and immunohistochemistry, indicating dysfunction of the ASS1/arginine axis in the pathology of UC. In vivo experiments demonstrate that genetic downregulation of ASS1 and pharmacological inhibition of arginine biosynthesis reduce colonic inflammation and pathological symptoms in mice with colitis by inhibiting mTOR-related pathways. Conversely, overexpression of ASS1 or supplementation with arginine exacerbates colitis in mice through mTOR overactivation, indicating that the ASS1/arginine axis is specifically upregulated in the colon during colitis. Notably, we screen ~1.6 million compounds and identify C-01, a highly potent ASS1 inhibitor that significantly improves symptoms in UC mouse models, suggesting that ASS1 inhibitors could offer therapeutic options for UC. These findings suggest that targeting the ASS1/arginine axis through genetic or pharmacological intervention may represent a promising therapeutic strategy for preventing and treating UC.

Results

Establishment of multi-center cohorts for human ulcerative colitis

We established multi-center human Ulcerative Colitis (UC) cohorts across three hospitals in China (Fig. 1a, “Methods”). Briefly, at the first hospital, we recruited 131 UC participants and 127 age- and sex-matched healthy control participants, designating this as the discovery cohort. Subsequently, an additional independent cohort was constructed at the same hospital, comprising 141 UC participants and 136 age- and sex-matched healthy controls, labeled as validation cohort 1. Validation cohorts 2 and 3 were established at the second and third hospitals, including 30 UC participants and 30 age- and sex-matched healthy control participants, respectively. Blood samples were collected from all participants upon enrollment. In addition, we obtained inflamed and corresponding normal colonic mucosal biopsies (colon tissue samples) and faeces from participants in the discovery cohort (Fig. 1a). In addition, we collected detailed demographic data for all participants across four cohorts (Fig. 1b and Supplementary Fig. 1a), with comprehensive information provided in Supplementary Tables 1, 6–8. To minimize the impact of confounders, as we mentioned above, we recruited healthy control participants who were matched in age and sex to the UC participants. As a result, in the discovery cohort, there were no significant differences in sex (chi-square test, $p = 0.54$, Fig. 1c), age (Wilcoxon test, $p = 0.53$, Fig. 1c), or BMI (Wilcoxon test, $p = 0.11$, Fig. 1c) between the control and UC participants. This lack of statistical significance was consistent across all validation cohorts (Supplementary Fig. 1b).

Untargeted metabolomics data from the discovery cohort was then acquired, yielding 9757 metabolic features (Fig. 1d). The quality of the data was thoroughly evaluated using various methods, all of which confirmed the high quality of the dataset (Supplementary Fig. 2a–d). As outlined in Fig. 1e, our data analysis strategy began with identifying differential metabolic features between the healthy control and UC participants, followed by identifying these metabolic features using LC-MS/MS. Pathway enrichment analysis was conducted to determine the enriched pathways based on the identified differential metabolites.

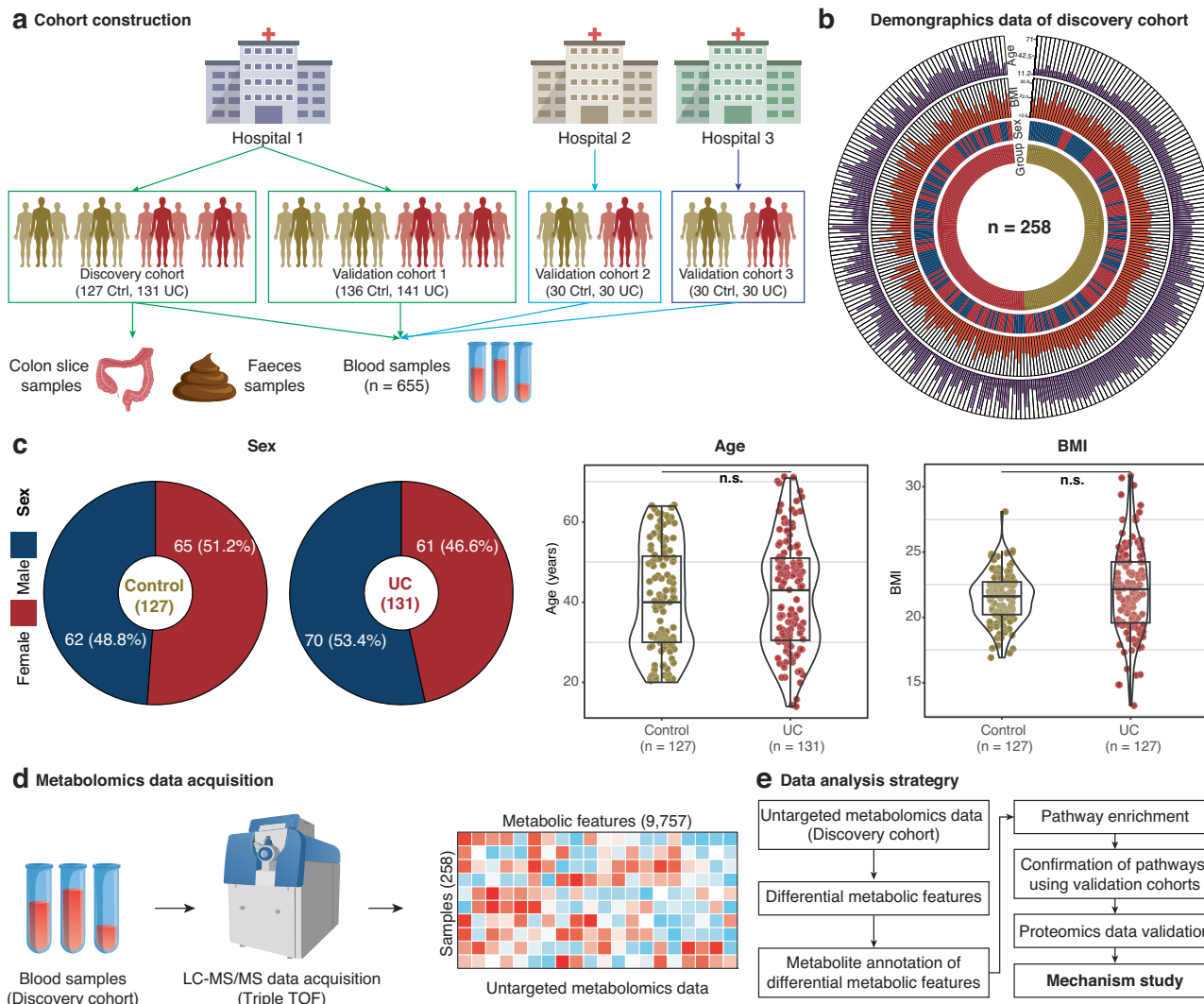


Fig. 1 | Establishment of multi-center human UC cohorts. **a** A discovery cohort and three independent validation human UC cohorts were established at three hospitals. **b** Demographic data of all participants in the discovery cohort, including sex, age, and BMI. **c** The statistical comparison shows no significant differences in sex, age, and BMI between healthy controls and UC participants in the discovery

cohort (sex: $P > 0.05$, Chi-square test; age and BMI: $P > 0.05$, Mann-Whitney U test). Box plots show the center line as median, whiskers show maxima and minima, and box limits show upper and lower quartiles. **d** Acquisition of untargeted metabolomics data for the discovery cohort. **e** Overview of the data analysis strategy used in the study. UC, ulcerative colitis; BMI, Body Mass Index.

These findings were subsequently validated using additional cohorts and cross-verified with proteomics data from colon tissues. Finally, *in vivo* and *in vitro* experiments will be employed to explore the underlying mechanisms, informed by the multi-omics data from our multi-center human UC cohorts.

Multi-omics data show higher arginine and the rate-limiting biosynthetic enzyme (ASS1) in UC patients

To investigate the relevance of the metabolic profile to the pathological processes of UC, we conducted a comparative analysis of serum untargeted metabolomics in the discovery cohort. As shown in Fig. 2a, we identified 441 differentially expressed metabolic features, with 216 upregulated and 225 downregulated in UC patients. The t-distributed Stochastic Neighbor Embedding (t-SNE) approach was then used to explore the separation between the two groups. The t-SNE could reduce the dimensionality of the data while retaining the essential structure and relationships between samples²⁶. The t-SNE plot demonstrates that the metabolic profiles of UC participants and control participants form distinct clusters. This indicates that the 441 differential metabolic features have distinct patterns between the two

groups, effectively separating UC patients from healthy controls (Fig. 2b). We then employed the LC-MS/MS method to identify these 441 metabolic features, successfully identifying 53 metabolites, where 30 were in positive mode, and 23 were in negative mode (Fig. 2c and Supplementary Tables 2, 3, and “Methods”). Notably, four metabolites were identified in both modes, and the metabolite with the higher median intensity was selected for further analysis (Fig. 2d). This process resulted in a final set of 49 differentially expressed metabolites, such as arginine and glutamate, which were provided in the Supplementary Tables 2, 3.

Hierarchical clustering was then applied to the 49 differentially expressed metabolites, resulting in two distinct clusters (Fig. 2e). Most of these metabolites were consistent with the findings from the volcano plot (Fig. 2a). Next, we explored the dysregulated metabolic pathways using KEGG pathway enrichment analysis, identifying several pathways, including the mTOR signaling pathway (Fig. 2f). Given that we also have Mayo scores for all UC patients, which indicate the severity of UC patients, we calculated Pearson correlations between metabolite intensities and Mayo scores (Fig. 2g). As anticipated, the fold changes (UC/Control) of the metabolites were strongly consistent

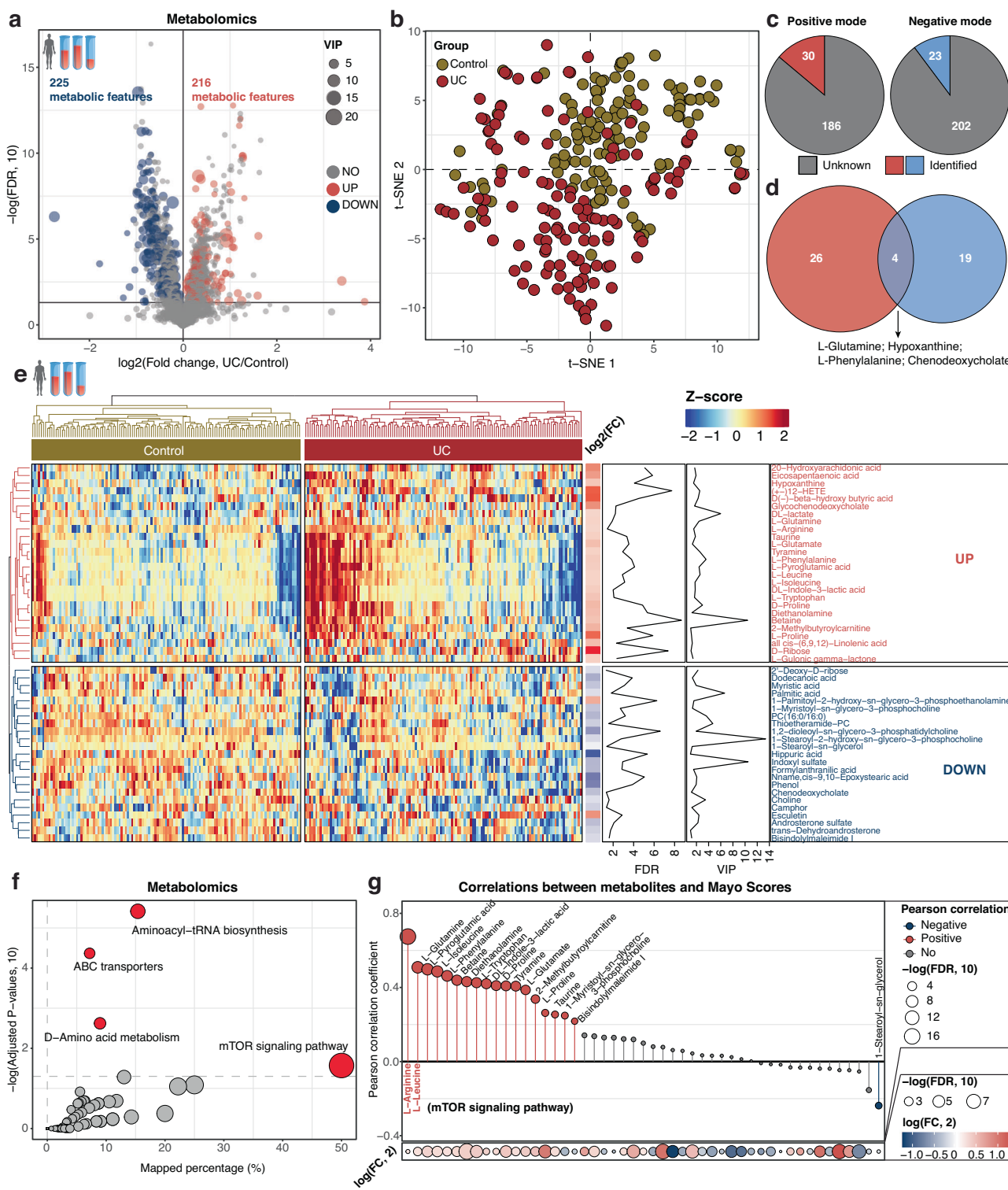


Fig. 2 | Distinct metabolic profiling between control and UC participants. **a** 441 differentially expressed metabolic features from serum samples were identified between control and UC participants. **b** t-SNE analysis shows that control and UC participants can be separated in the plot, indicating that these metabolic features from serum samples can effectively separate UC patients from healthy individuals based on their overall metabolic profiles. **c** 53 differentially expressed metabolic features from serum samples were identified as specific metabolites. **d** Four

metabolites were detected in both positive and negative ionization modes. **e** Hierarchical clustering groups all differential metabolites from serum samples into two classes, closely aligning with the results of the volcano plot. **f** Pathway enrichment analysis reveals significant enrichment of the mTOR signaling pathway in serum samples. **g** Pearson correlation analysis between serum metabolites and Mayo scores of UC patients indicates that two metabolites from the mTOR pathway are among the top-ranked. UC, ulcerative colitis.

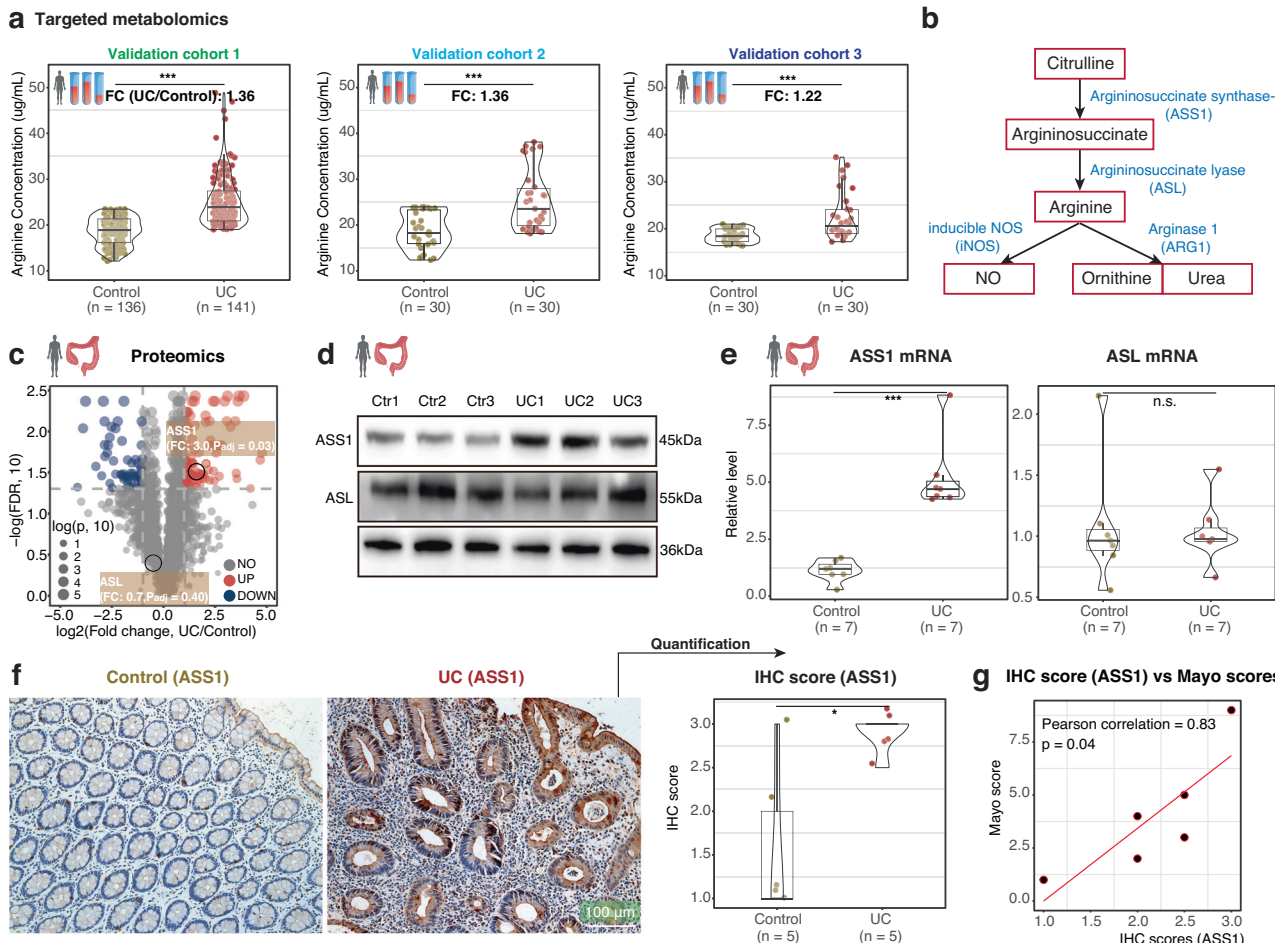


Fig. 3 | Elevated levels of arginine and ASS1 in human UC patients. **a** Targeted metabolomics of serum from three independent validation human cohorts confirm that arginine levels are higher in UC patients. $p < 2.2e-16$ for validation cohort 1, $p = 3.78e-05$ for validation cohort 2, $p = 7.22e-05$ for validation cohort 3. Comparisons were performed using the Mann-Whitney U test. **b** The metabolism pathway of arginine. **c** Proteomics data from colonic tissues in the discovery cohort show significant upregulation of ASS1, the rate-limiting enzyme in arginine biosynthesis, in UC patients. **d** Western blot analysis reveals a significant increase in ASS1 levels in colonic tissues from healthy controls and UC patients

(Quantitative analysis shown in Supplementary Fig. 7). **e** RT-PCR results indicate a significant increase in *ASS1* mRNA levels in colonic tissues from healthy controls and UC patients ($p = 5.83e-04$, Mann-Whitney U test), while *ASL* levels remain unchanged. **f** Immunohistochemistry (IHC) shows a significant elevation of ASS1-positive cells in the colon slices of UC patients compared to control normal participants ($p = 0.029$, Welch's *t* test). **g** IHC scores are highly correlated with Mayo scores in UC patients (Pearson correlation = 0.83, $p = 0.04$). Box plots show the center line as median, whiskers show maxima and minima, and box limits show upper and lower quartiles. UC, ulcerative colitis.

with the Pearson correlations (Fig. 2g and Supplementary Tables 4, 5). Notably, the two metabolites with the highest positive correlations were arginine ($r = 0.67$, $fdr = 5.32 \times 10^{-17}$) and leucine ($r = 0.51$, $fdr = 1.44 \times 10^{-18}$), both of which are components of the mTOR pathway (Fig. 2f). These findings indicate that the mTOR signaling pathway, particularly arginine, is activated in UC patients.

To confirm and validate the upregulation of arginine in UC patients, targeted metabolomics analysis was conducted across three independent validation human UC cohorts (Fig. 1a). As anticipated, circulating arginine levels in serum were significantly elevated in all three human cohorts (Fig. 3a). In addition, we observed that arginine levels were also elevated in fecal samples of UC patients within the discovery cohort (Supplementary Fig. 3a and Table 9). These findings collectively demonstrate that arginine is significantly upregulated in both serum and fecal samples of UC patients.

Next, we aimed to investigate how the arginine metabolism pathway is altered in UC patients. It is well known that argininosuccinate synthase-1 (ASS1) catalyzes the conversion of citrulline to argininosuccinate, which is then converted to arginine by argininosuccinate lyase (ASL)^{27,28}. Arginine can subsequently be converted to nitric oxide

(NO) by nitric oxide synthase (inducible nitric oxide synthase [iNOS] and endothelial nitric oxide synthase [eNOS]) or metabolized into ornithine and urea by the bimetallic enzyme arginase 1 (ARG1)²⁹ (Fig. 3b).

We, therefore, examined the levels of arginine-related metabolites in UC patients. We found that the intermediate metabolite argininosuccinate was significantly elevated in the serum samples of UC patients (Supplementary Fig. 3b, c). In addition, the downstream metabolites of arginine, including ornithine and nitric NO, were significantly upregulated in UC patients' serum, while urea levels remained unchanged (Supplementary Fig. 4 and Table 10). Consistently, the mRNA levels of *ARG1* and *NOS2* were raised in UC patients and colitis mice (Supplementary Fig. 5a-d).

In addition, we conducted label-free proteomics to analyze differential protein expression in UC patients using five normal controls and five colonic mucosal biopsies (Supplementary Fig. 6 and Supplementary Table 11). As expected, ASS1 protein was significantly upregulated in the colon tissue samples of UC patients compared to healthy normal tissue samples (FC: 3.2, $p < 0.0001$), while ASL protein remained unchanged (FC: 0.9, $p = 0.99$, Fig. 3c), which were also

confirmed using Western blot experiment (Fig. 3d, Supplementary Fig. 7 and Supplementary Table 12). RT-PCR experiments corroborated these findings, showing significant upregulation of ASS1 mRNA in UC patients' colon tissue, with no change in ASL mRNA levels (Fig. 3e and Supplementary Table 12). The upregulation of ASS1 and unchanged ASL expression in UC patients were further validated by GEO analysis of four public UC datasets (GSE75214, GSE87473, GSE47908, and GSE128682), which consistently demonstrated significant ASS1 upregulation in UC patients, with no change in ASL levels (Supplementary Figs. 8, 9). To further confirm the upregulation of ASS1 in UC patients, immunohistochemistry (IHC) of colon tissues was performed, revealing a significant increase in ASS1-positive cells in UC patients' colon tissue (Fig. 3f and Supplementary Table 13). In addition, similar to the correlation between arginine levels and Mayo scores in UC patients, the IHC scores of ASS1 were also positively correlated with Mayo scores ($r=0.83$, $p=0.04$) in six colon samples from UC patients (Fig. 3g, Supplementary Fig. 10 and Table 14). Overall, these results strongly suggest that arginine and its rate-limiting biosynthetic enzyme ASS1 are significantly upregulated in UC patients, and they may play critical pathological roles in the development and progression of UC.

Exogenous arginine exacerbates clinical outcomes in the UC mouse models

We have demonstrated that arginine and its rate-limiting biosynthetic enzyme ASS1 are significantly upregulated in UC patients using metabolomics and proteomics data. Next, we aimed to investigate whether arginine is involved in the pathology of UC and to explore the underlying mechanisms. To achieve this, we established a UC mouse model using dextran sulfate sodium (DSS) ("Methods"). Compared to control mice, the UC mouse models showed a significant and rapid reduction in body weight, an increase in disease activity index (DAI), and a reduction in colon length - effects further exacerbated in UC mouse models supplemented with arginine (Fig. 4a).

We then measured arginine levels in the mice. As expected, arginine levels were significantly elevated in the serum and colon tissues of both UC mouse models and those supplemented with arginine (Fig. 4b). Furthermore, histopathological analysis of colon tissues revealed that arginine supplementation markedly increased inflammatory cell infiltration and mucosal damage in the UC mouse models (Fig. 4c). Interestingly, arginine administration had no effect on the colonic histology in control mice (Supplementary Fig. 11). Consistent with the histopathological findings, myeloperoxidase (MPO) levels and proinflammatory cytokines, including IL-6 and IL-1 β , were significantly elevated in the colon tissues of UC mouse models supplemented with arginine (Fig. 4d). These results demonstrate that arginine has proinflammatory effects and exacerbates clinical outcomes in the UC mouse models.

It is well-established that mTOR overactivation is a driving force in the development of UC³⁰, and arginine is a well-known direct activator of mTOR²⁴. Therefore, we hypothesized that arginine may contribute to the pathogenesis of UC through an mTOR-dependent mechanism. To test this hypothesis, we examined the levels of phosphorylated mTOR and its associated signaling pathways in colon tissues. As expected, immunoblotting revealed significant upregulation of phosphorylated mTOR, STAT3, and S6, along with increased expression of ASS1 and COX-2 proteins in the colon tissues of UC mouse models. These effects were even more pronounced in the UC mouse models supplemented with arginine (Fig. 4e). These findings suggest that arginine may activate the mTOR pathway, thereby promoting the onset and progression of UC in mice. Besides, in order to evaluate the relationship between arginine and gut microbiota, we performed 16S rDNA sequencing analysis on fecal samples from control, model, and model + arginine groups. Administration of arginine significantly affected the α -diversity using Chao1 and Shannon (Supplementary

Fig. 12a, b). The principal coordinate analysis (PCoA) revealed a fecal microbial separation among the three groups (Supplementary Fig. 12c). In addition, the linear discriminant analysis effect size (LEfSe) showed that the abundance of the genera butyrate-producing *clostridium* and *oscillibacter* was significantly decreased, and further reduced after administration of arginine (Supplementary Fig. 12d-h). These findings indicate that arginine contributes to colitis development by partially regulating the gut microbiome.

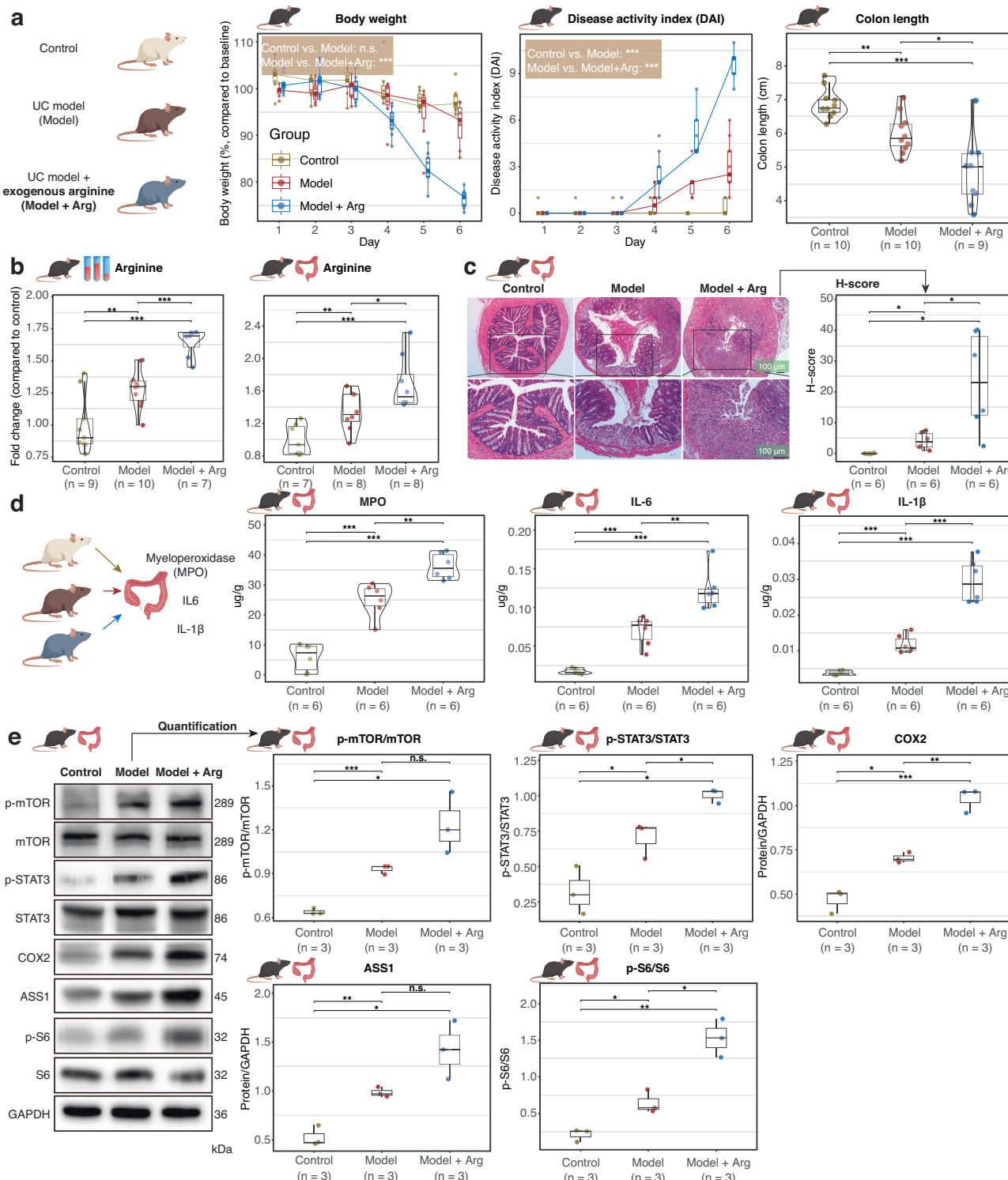
Manipulation of arginine synthesis significantly affects the clinical outcomes of the UC mouse models

As we previously demonstrated, the protein level of ASS1 is significantly upregulated in UC patients, prompting us to investigate whether modulating ASS1 expression could influence the development of UC. To investigate this, we established a UC mouse model with colonic ASS1 overexpression by administering AAV-ASS1 via enema infusion. We then assessed ASS1 protein expression and arginine production in colonic tissues. The protein expression of ASS1 began to upregulate at 2 weeks and continued to enhance until 6 weeks after the duration of ASS1 overexpression (Supplementary Fig. 13). The protein expression of ASS1 was not changed in the spleen, heart, lungs, liver, or kidneys (Supplementary Fig. 13). IHC analysis confirmed a marked upregulation of ASS1 expression in the colon following AAV-mediated overexpression (Supplementary Fig. 14). These results confirm that our ASS1 OE mouse models were successfully established, leading to the overexpression of ASS1, specifically in the colon tissues.

Not surprisingly, ASS1 overexpression resulted in similar and significant effects on body weight, DAI, and colonic shortening in the UC mouse models (Fig. 5a), indicating that ASS1 overexpression exacerbates clinical outcomes in the UC mouse models. Consistent with these findings, histopathological analysis of colon tissues further confirmed that ASS1 overexpression worsened inflammatory cell infiltration and mucosal damage in UC mouse models (Supplementary Fig. 15a, b). Moreover, the levels of proinflammatory cytokines (MPO, IL-6, and IL-1 β) were further aggravated in response to ASS1 overexpression (Supplementary Fig. 15c-e), along with increased protein expressions of P-mTOR, P-STAT3, P-S6, and COX-2 (Supplementary Fig. 15f). Overexpression of ASS1 was sufficient to yield more arginine in mice upon exposure to DSS (Supplementary Fig. 15g, h).

We then established the ASS1 gene deletion UC mouse models. As expected, the deletion of ASS1 significantly resulted in downregulated ASS1 protein expression, specifically in the colon tissue, with no significant changes observed in the spleen, heart, lungs, liver, or kidneys (Supplementary Fig. 16). IHC analysis of colonic tissue further demonstrated that ASS1 expression was significantly reduced following AAV-mediated delivery of ASS1-targeting shRNA (Supplementary Fig. 17). In stark contrast to the ASS1 overexpression models, ASS1 deletion exhibited opposite phenotypes, alleviating clinical symptoms in the UC mouse models (Fig. 5b). Histopathological analysis of colon tissues further confirmed that ASS1 deletion alleviated inflammatory cell infiltration and mucosal damage in ASS1 deletion UC mouse models (Supplementary Fig. 18a, b). The levels of proinflammatory cytokines were also reduced in the ASS1 deletion models (Supplementary Fig. 18c-e), along with decreased protein expression of P-mTOR, P-STAT3, P-S6, and COX-2 (Supplementary Fig. 18f). The arginine was also significantly downregulated in the serum of ASS1 deletion UC mouse models (Supplementary Figs. 18g, h).

To further investigate the manipulation of arginine, we utilized a well-established ASS1 inhibitor, α -methyl-dl-aspartic acid (MDLA)³¹⁻³³, to downregulate arginine levels in the UC mouse models. The root mean square deviation (RMSD) of ASS1 backbone atoms and MDLA during molecular dynamics simulation showed that the RMSD increased to 2.5 Å within 50 ns and then stabilized at approximately 3 Å (Fig. 5c). As shown in Fig. 5d, MDLA formed multiple hydrogen bonds with ASS1 by interacting with Tyr87, Asn123, Arg127, Glu190, Glu269,



and Arg271. The binding energy, calculated using the Molecular Mechanics-Poisson Boltzmann Surface Area (MM-PBSA) method, was -31.56 kcal/mol (Fig. 5d). Consistent with the ASS1 deletion experiments, ASS1 inhibition with MDLA also alleviated clinical outcomes in the UC mouse models (Fig. 5e). In addition, histopathological analysis of colon tissues further confirmed that ASS1 inhibition with MDLA alleviated inflammatory cell infiltration and mucosal damage (Supplementary Fig. 19a, b), reduced inflammatory cell infiltration and multiple ulcers in colon tissues (Supplementary Fig. 19c–e), and decreased levels of phosphorylated mTOR, STAT3, S6, and COX-2 in the colon tissues (Supplementary Fig. 19f). ASS1 inhibition with MDLA

successfully significantly downregulated the arginine levels in colon and serum samples (Supplementary Fig. 19g, h). In summary, these *in vivo* experiments demonstrate that manipulating arginine levels through ASS1 modulation plays a critical role in the etiology of UC.

Effects of the ASS1/Arginine Axis on the mTOR signaling pathway and inflammation in cells

Based on the previous experiments and results, we hypothesize that the upregulation of ASS1 in UC patients leads to increased arginine levels, which in turn activate the mTOR pathway. This activation promotes the expression of pro-inflammatory factors, thereby

Fig. 4 | Exogenous arginine exacerbates clinical outcomes in the UC mouse models. **a** Exogenous arginine (Arg) exacerbates clinical outcomes in the UC mouse model, including body weight loss, increased disease activity index, and reduced colon length. Body weight: Control vs Model ($p = 0.061$), Model vs Arg ($p = 6.67e-04$). Disease activity index: Control vs Model ($p = 8.16e-05$), Model vs Arg ($p = 2.13e-08$). Colon length: Control vs DSS ($p = 0.001$), Control vs Arg ($p = 2.33e-04$), DSS vs Arg ($p = 0.013$). Body weight and disease activity index were analyzed using repeated measures ANOVA; colon length was compared using Welch's *t* test. ($n = 10$ for Control, $n = 10$ for Model, $n = 9$ for Model + Arg). **b** Arginine levels significantly increase in colon tissues (left) and blood (right) in both the UC mouse and arginine-administered UC mouse models. For blood arginine: Control vs Model ($p = 0.007$), Control vs Arg ($p = 6.38e-06$), Model vs Arg ($p = 4.93e-05$). For colon arginine: Control vs Model ($p = 0.008$), Control vs Arg ($p = 3.72e-04$), Model vs Arg ($p = 0.035$). Comparisons were performed using Welch's *t* test. **c** Histopathological analysis of colon tissues reveals that arginine supplementation significantly promotes inflammatory cell infiltration and mucosal damage in UC mouse models. H-score analysis: Control vs Model ($p = 0.014$), Control vs Arg ($p = 0.016$), Model vs Arg ($p = 0.031$). Comparisons were performed using Welch's *t* test. **d** Myeloperoxidase activity and proinflammatory cytokines (IL-6 and IL-1 β) significantly increase in colon tissues of both UC mouse models and

arginine-supplemented UC mouse models. MPO: Control vs Model ($p = 8.99e-05$), Control vs Arg ($p = 3.60e-07$), Model vs Arg ($p = 0.003$). IL-6: Control vs Model ($p = 9.48e-04$), Control vs Arg ($p = 1.72e-04$), Model vs Arg ($p = 0.003$). IL-1 β : Control vs Model ($p = 3.64e-04$), Control vs Arg ($p = 1.29e-04$), Model vs Arg ($p = 3.83e-04$). Comparisons were performed using Welch's *t* test. **e** Immunoblotting results show that the levels of phosphorylated mTOR, STAT3, and S6, as well as the expressions of ASS1 and COX-2 proteins, are significantly elevated in the colon tissues of UC mouse models, with more severe effects observed after arginine supplementation. p-mTOR/mTOR: Control vs Model ($p = 3.93e-04$), Control vs Arg ($p = 0.038$), Model vs Arg ($p = 0.126$). p-STAT3/STAT3: Control vs Model ($p = 0.041$), Control vs Arg ($p = 0.014$), Model vs Arg ($p = 0.042$). COX-2: Control vs Model ($p = 0.015$), Control vs Arg ($p = 5.17e-04$), Model vs Arg ($p = 0.007$). ASS1: Control vs Model ($p = 0.008$), Control vs Arg ($p = 0.025$), Model vs Arg ($p = 0.122$). p-S6/S6: Control vs Model ($p = 0.022$), Control vs Arg ($p = 0.008$), Model vs Arg ($p = 0.013$). Comparisons were performed using Welch's *t* test. Box plots show the center line as the median, whiskers show the maxima and minima, and box limits show the upper and lower quartiles. UC, ulcerative colitis; MPO, myeloperoxidase; IL-6, Interleukin-6; IL-1 β , Interleukin 1 β ; mTOR, mammalian target of rapamycin; STAT3, signal transducer and activator of transcription 3; S6, Ribosomal protein S6; COX-2, Cyclooxygenase-2; ASS1, argininosuccinate synthetase 1.

exacerbating the clinical outcomes of UC. To test this hypothesis *in vitro*, we used IL-6 to stimulate normal human colon mucosal epithelial cell lines (NCM460 cells) to mimic inflammatory colitis. We then investigated whether modulating arginine levels could influence the mTOR signaling pathway and the release of inflammatory factors. Pre-incubation with MDLA or silencing of ASS1 provided protective effects, reducing IL-6-induced mTOR activation and IL-1 β release (Supplementary Fig. 20). Similar results were observed in primary intestinal epithelial cells (Supplementary Fig. 21). Collectively, these *in vivo* and *in vitro* experiments demonstrate that the ASS1/Arginine Axis plays a crucial role in the development and progression of UC by activating the mTOR pathway. In addition, we also used intestinal organoids derived from humans to further confirm our NCM460 cell results. Results showed that both C-01 and MDLA reduced the phosphorylation level of mTOR, STAT3, and S6, as well as suppressed the protein expression of COX2 in cultured human intestinal organoids (Supplementary Fig. 22, 23). Moreover, HE staining showed that the injury in human intestinal organoids was significantly prevented by C-01 and MDLA (Supplementary Fig. 24a, c). The suppressive effects of C-01 and MDLA on the protein expression of COX2 were also ascertained by IHC in human intestinal organoids (Supplementary Fig. 24b, d).

Effects of eNOS and iNOS inhibition on the role of arginine in colitis

As shown in Supplementary Fig. 25a, serum NO production was elevated in DSS-induced mice and was further enhanced in the presence of arginine. Supplementation of arginine further potentiated the effects of DSS on the protein and mRNA levels of *iNOS* in the colon (Supplementary Fig. 25b, c). Interestingly, the utilization of arginine had no effect on the expression of eNOS (Supplementary Fig. 25d, e). Collectively, exogenous arginine might drive the development of colitis by partially inducing iNOS in intestinal epithelial cells. To further confirm this hypothesis, we conducted cellular and animal experiments using inhibitors of eNOS/iNOS or their siRNAs. At cellular levels, silencing iNOS prevented the protein expression of iNOS and COX-2, as well as NO generation in IL-6 induced NCM460 cells co-treated with arginine (Supplementary Fig. 26a, b). Intriguingly, the knockdown of eNOS was unable to affect the actions of arginine on the protein expression levels of COX-2 and NO formation in NCM460 cells exposed to IL-6 (Supplementary Fig. 26c, d). In colitis mice, administration of a specific iNOS inhibitor, 1400 W Dihydrochloride, rather than a specific eNOS inhibitor, carboxyebseLEN, attenuated the effects of arginine on UC development in mice (Supplementary Fig. 27). In

summary, these results indicated that arginine drives the development of colitis, partially dependent on iNOS.

Epigenetic regulation of ASS1 expression in UC

Next, we aimed to explore the regulation mechanism of ASS1 expression in UC. Consistent with the changes in the protein expression of ASS1, IL-6 stimulation upregulated the transcriptional level of ASS1 (Fig. 6a). To evaluate whether IL-6-induced ASS1 transcription was related to alterations in the chromatin structure, we conducted a series of ChIP analyses. In response to IL-6 stimulation, acetylated histone H3 and trimethylated H3K4, which are usually associated with active chromatin, were recruited to the ASS1 promoters (Fig. 6b-d). In contrast, acetyl H3 and trimethyl H3K4 levels remained unchanged within the ASS1 intronic region (Fig. 6b-d). Besides, dimethylated H3K9, a signature histone mark that represents repressed chromatin, receded from the ASS1 promoter region following IL-6 treatment (Fig. 6e). However, exposure to IL-6 did not affect the accumulation of trimethylated H3K27 surrounding the CSF1 promoter (Fig. 6c). A previous study demonstrated that the constant attachment of the transcription factor c-Myc to the ASS1 promoter resulted in the increased transcription of ASS1 during glucose deprivation³². Thus, the potential transcription factor c-Myc was identified to be located within the promoter of ASS1 using the JASPER database (Fig. 6f, g). Importantly, c-Myc depletion not only prevented IL-6-induced upregulation of ASS1 (Fig. 6h, i), but also changed the chromatin structure within the ASS1 promoters in response to IL-6, such as decreasing acetylated H3 and trimethylated H3K4 (Fig. 6j, k), and increasing accumulation of dimethylated H3K9 surrounding the ASS1 promoter region (Fig. 6l). Interestingly, co-immunoprecipitation experiments showed that KDM3A, an H3K9 demethylase, and p300, a histone acetyltransferase, formed a complex with c-Myc, and the complex formation was more pronounced in the absence of IL-6, thus driving the transcriptional activation of ASS1 in UC (Fig. 6m, n).

Screening identifies C-01 as an inhibitor of ASS1

According to the previous studies, we demonstrated that ASS1 is a potential target for UC therapy, and we proposed a computer-aided drug design strategy to screen ASS1 inhibitors to cure UC. The strategy involved virtual screening, molecular dynamics simulation, and experimental validation (Fig. 7a). Briefly, the molecular operating environment was used to dock 1.6 million compounds from the ChemDiv library and to score their potential complementarity with putative binding sites in the human ASS1 structure. After docking, the top 500 ligands based on the lowest binding energies were selected for

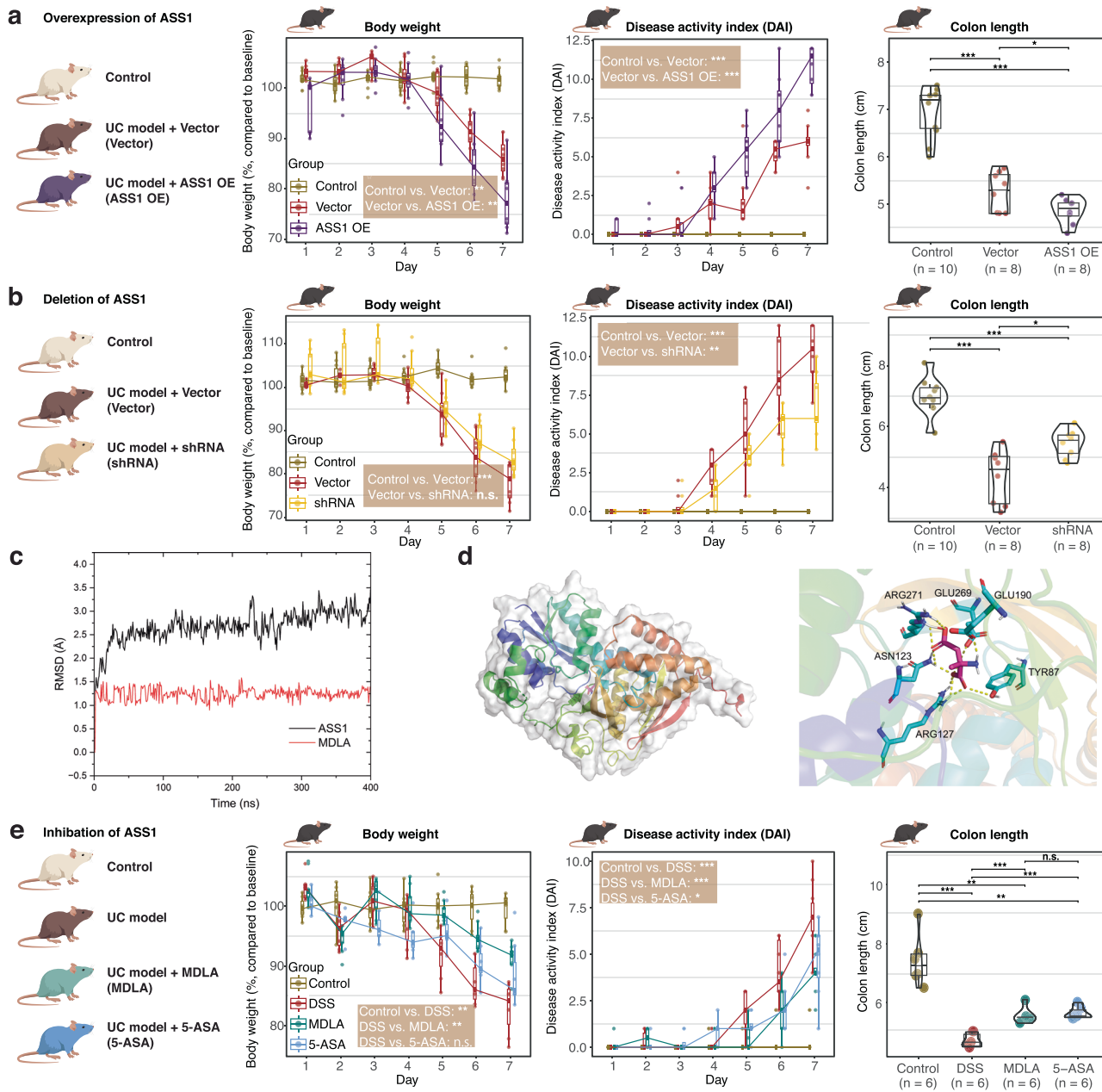


Fig. 5 | Modulation of arginine synthesis exacerbates or alleviates clinical outcomes in UC mouse models. **a** Overexpression of ASS1 exacerbates clinical outcomes in the UC mouse model, including body weight loss, increased disease activity index, and reduced colon length. Body weight: Control vs Vector ($p = 0.002$), Vector vs ASS1 OE ($p = 0.002$). Disease activity index: Control vs Vector ($p = 7.06e-10$), Vector vs ASS1 OE ($p = 2.65e-05$). Colon length: Control vs Vector ($p = 1.62e-06$), Control vs ASS1 OE ($p = 5.25e-08$), Vector vs ASS1 OE ($p = 0.044$). Body weight and disease activity index were analyzed using repeated measures ANOVA; colon length was compared using Welch's *t* test ($n = 10$ for Control, $n = 8$ for Vector, $n = 8$ for ASS1 OE). **b** Deletion of ASS1 alleviates clinical outcomes in UC mouse models. Body weight: Control vs Vector ($p = 1.62e-06$), Vector vs shRNA ($p = 0.060$). Disease activity index: Control vs Vector ($p = 2.49e-09$), Vector vs shRNA ($p = 0.006$). Colon length: Control vs Vector ($p = 1.18e-05$), Control vs shRNA ($p = 1.20e-05$), Vector vs shRNA ($p = 0.011$). Body weight and disease activity index were analyzed using repeated measures ANOVA; colon length was compared using Welch's *t* test ($n = 10$ for Control, $n = 8$ for Vector, $n = 8$ for shRNA). **c** Root mean square deviation (RMSD) of protein backbone atoms and MDLA during the MD simulation. **d** Molecular docking and the binding mode of MDLA to ASS1 through molecular dynamics (MD) simulation. **e** Inhibition of ASS1 using MDLA also alleviates clinical outcomes in UC mouse models. Body weight: Control vs DSS ($p = 0.001$), DSS vs MDLA ($p = 0.005$), DSS vs 5-ASA ($p = 0.630$). Disease activity index: Control vs DSS ($p = 4.15e-07$), DSS vs MDLA ($p = 2.08e-04$), DSS vs 5-ASA ($p = 0.026$). Colon length: Control vs DSS ($p = 0.0004$), Control vs MDLA ($p = 0.003$), Control vs 5-ASA ($p = 0.004$), DSS vs MDLA ($p = 0.0002$), DSS vs 5-ASA ($p = 2.61e-05$), MDLA vs 5-ASA ($p = 0.566$). Body weight and disease activity index were analyzed using repeated measures ANOVA; colon length was compared using Welch's *t* test ($n = 6$ for Control, $n = 6$ for DSS, $n = 6$ for MDLA, $n = 6$ for 5-ASA). Box plots show the center line as the median, whiskers show maxima and minima, and box limits show upper and lower quartiles. UC, ulcerative colitis; MDLA, α -Methyl-DL-aspartic acid; ASS1, argininosuccinate synthetase 1. 5-ASA, 5-aminosalicylic acid.

Welch's *t* test ($n = 10$ for Control, $n = 8$ for Vector, $n = 8$ for shRNA). **c** Root mean square deviation (RMSD) of protein backbone atoms and MDLA during the MD simulation. **d** Molecular docking and the binding mode of MDLA to ASS1 through molecular dynamics (MD) simulation. **e** Inhibition of ASS1 using MDLA also alleviates clinical outcomes in UC mouse models. Body weight: Control vs DSS ($p = 0.001$), DSS vs MDLA ($p = 0.005$), DSS vs 5-ASA ($p = 0.630$). Disease activity index: Control vs DSS ($p = 4.15e-07$), DSS vs MDLA ($p = 2.08e-04$), DSS vs 5-ASA ($p = 0.026$). Colon length: Control vs DSS ($p = 0.0004$), Control vs MDLA ($p = 0.003$), Control vs 5-ASA ($p = 0.004$), DSS vs MDLA ($p = 0.0002$), DSS vs 5-ASA ($p = 2.61e-05$), MDLA vs 5-ASA ($p = 0.566$). Body weight and disease activity index were analyzed using repeated measures ANOVA; colon length was compared using Welch's *t* test ($n = 6$ for Control, $n = 6$ for DSS, $n = 6$ for MDLA, $n = 6$ for 5-ASA). Box plots show the center line as the median, whiskers show maxima and minima, and box limits show upper and lower quartiles. UC, ulcerative colitis; MDLA, α -Methyl-DL-aspartic acid; ASS1, argininosuccinate synthetase 1. 5-ASA, 5-aminosalicylic acid.

further analysis. By inspecting the interaction patterns of each ligand bound to ASS1, 11 compounds (C-01 to C-11, Supplementary Table 15) that formed reasonable hydrogen bonds with ASS1 were obtained. Among the 11 compounds, pretreatment with C-01 and C-02 (100 μ M)

effectively suppressed the phosphorylation of STAT3 in IL-6-exposed NCM460 cells. Further studies revealed that 500 nM C-01, rather than C-02, showed similar inhibitory effects on P-STAT3 in NCM460 cells challenged by IL-6 (Supplementary Fig. 28).

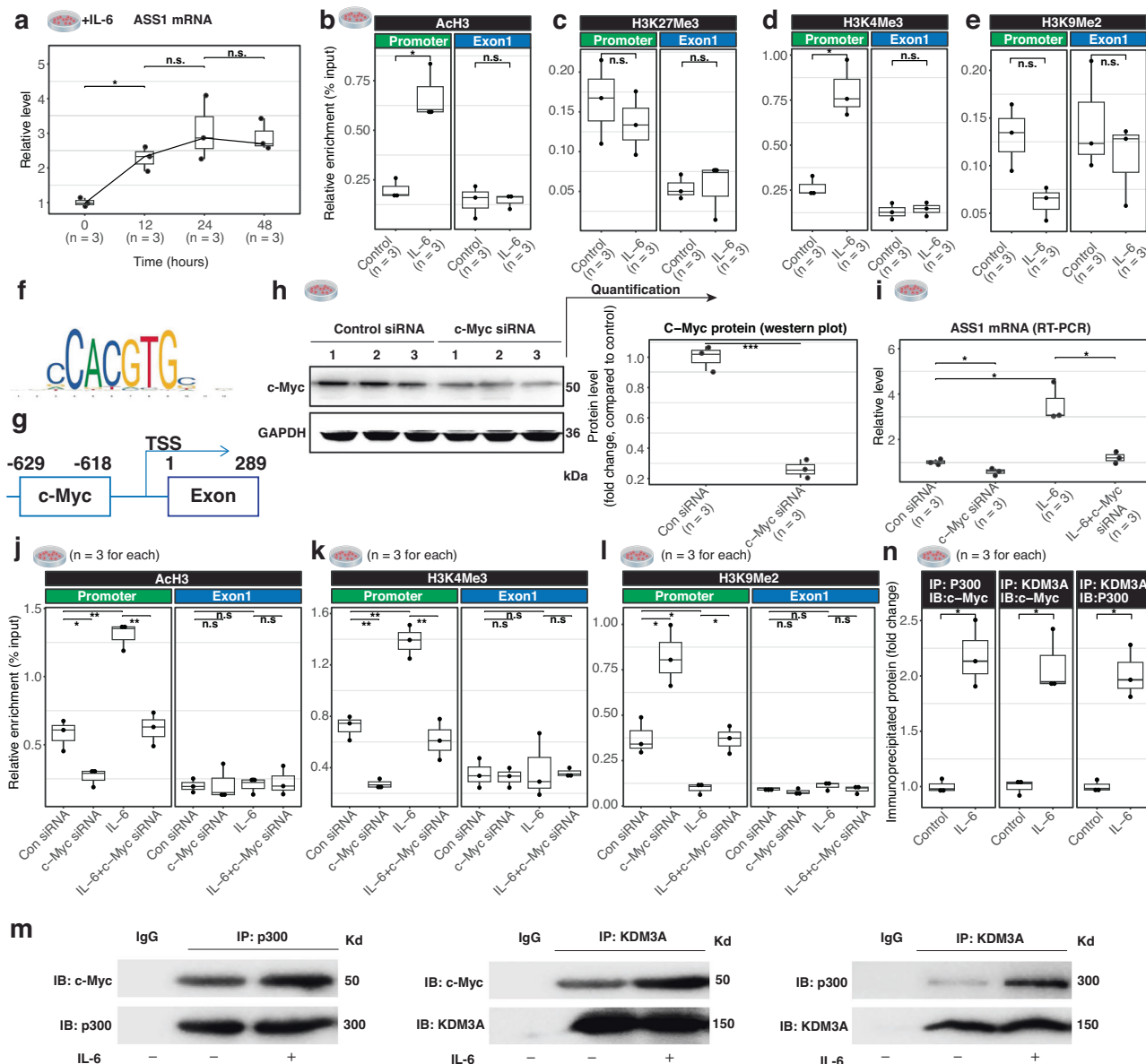


Fig. 6 | Epigenetic activation of ASS1 in colonic epithelial cells exposed to IL-6.

a Relative mRNA levels of ASS1 in IL-6-challenged NCM460 cells at indicated time points. 0 h vs 12 h ($p = 0.017$), 12 h vs 24 h ($p = 0.279$), 24 h vs 48 h ($p = 0.801$). Comparisons were performed using Welch's t test. NCM460 cells were treated with IL-6 and harvested for ChIP assays. ChIP assays were performed with (b), anti-acetyl H3, (c), anti-trimethyl H3K27, (d), anti-trimethyl H3K4, and (e), anti-dimethyl H3K9 surrounding ASS1 promoters.

b Anti-acetyl H3: Promoter region: Control vs IL-6 ($p = 0.019$); Exon1 region: Control vs IL-6 ($p = 0.994$). Comparisons were performed using Welch's t test.

c Anti-trimethyl H3K27: Promoter region: Control vs IL-6 ($p = 0.492$); Exon1 region: Control vs IL-6 ($p = 0.950$). Comparisons were performed using Welch's t test.

d Anti-trimethyl H3K4: Promoter region: Control vs IL-6 ($p = 0.019$); Exon1 region: Control vs IL-6 ($p = 0.715$). Comparisons were performed using Welch's t test.

e Anti-dimethyl H3K9: Promoter region: Control vs IL-6 ($p = 0.056$); Exon1 region: Control vs IL-6 ($p = 0.426$). Comparisons were performed using Welch's t test.

f The motif of c-Myc from the Jasper database.

g A schematic of the human ASS1 promoter highlighting the c-Myc site.

h Efficiency of control siRNA and c-Myc siRNA on the protein expression of c-Myc ($p = 3.99 \times 10^{-4}$). Comparison was performed using Welch's t test.

i Deficiency of c-Myc prevents IL-6-induced ASS1 mRNA expression. NCM460 cells were transfected with siRNA targeting c-Myc or random siRNA, followed by treatment with IL-6. Con siRNA vs c-Myc siRNA ($p = 0.020$), Con siRNA vs IL-6 ($p = 0.034$), IL-6 vs IL-6 + c-Myc siRNA ($p = 0.001$). Comparisons were performed using Welch's t test. ChIP assays were performed with (j) Anti-acetyl H3, (k) anti-trimethyl H3K4, and (l) anti-dimethyl H3K9 in NCM460 cells.

j Anti-acetyl H3: Promoter region: Con siRNA vs c-Myc siRNA ($p = 0.02$), Con siRNA vs IL-6 ($p = 0.001$), IL-6 vs IL-6 + c-Myc siRNA ($p = 0.001$). Exon region: all comparisons ($p > 0.1$).

k Anti-trimethyl H3K4: Promoter region: Con siRNA vs c-Myc siRNA ($p = 0.007$), Con siRNA vs IL-6 ($p = 0.003$), IL-6 vs IL-6 + c-Myc siRNA ($p = 0.003$). Exon region: all comparisons ($p > 0.1$).

l Anti-dimethyl H3K9: Promoter region: Con siRNA vs c-Myc siRNA ($p = 0.02$), Con siRNA vs IL-6 ($p = 0.03$), IL-6 vs IL-6 + c-Myc siRNA ($p = 0.01$). Exon region: all comparisons ($p > 0.1$).

m, **n** Effects of IL-6 on the complex formation of p300/c-Myc/KDM3A in NCM460 cells. IP: P300 IB: c-Myc ($p = 0.018$), IP: KDM3A IB: c-Myc ($p = 0.017$), IP: KDM3A IB: P300 ($p = 0.014$). Comparisons were performed using Welch's t test. All experiments were repeated three times. Error bars represent standard deviation. Con means control, Con siRNA means Control siRNA. Box plots show the center line as the median, whiskers show the maxima and minima, and box limits show upper and lower quartiles.

($p = 0.020$), Con siRNA vs IL-6 ($p = 0.034$), IL-6 vs IL-6 + c-Myc siRNA ($p = 0.001$). Comparisons were performed using Welch's t test. ChIP assays were performed with (j) Anti-acetyl H3, (k) anti-trimethyl H3K4, and (l) anti-dimethyl H3K9 in NCM460 cells.

j Anti-acetyl H3: Promoter region: Con siRNA vs c-Myc siRNA ($p = 0.02$), Con siRNA vs IL-6 ($p = 0.001$), IL-6 vs IL-6 + c-Myc siRNA ($p = 0.001$). Exon region: all comparisons ($p > 0.1$).

k Anti-trimethyl H3K4: Promoter region: Con siRNA vs c-Myc siRNA ($p = 0.007$), Con siRNA vs IL-6 ($p = 0.003$), IL-6 vs IL-6 + c-Myc siRNA ($p = 0.003$). Exon region: all comparisons ($p > 0.1$).

l Anti-dimethyl H3K9: Promoter region: Con siRNA vs c-Myc siRNA ($p = 0.02$), Con siRNA vs IL-6 ($p = 0.03$), IL-6 vs IL-6 + c-Myc siRNA ($p = 0.01$). Exon region: all comparisons ($p > 0.1$).

m, **n** Effects of IL-6 on the complex formation of p300/c-Myc/KDM3A in NCM460 cells. IP: P300 IB: c-Myc ($p = 0.018$), IP: KDM3A IB: c-Myc ($p = 0.017$), IP: KDM3A IB: P300 ($p = 0.014$). Comparisons were performed using Welch's t test. All experiments were repeated three times. Error bars represent standard deviation. Con means control, Con siRNA means Control siRNA. Box plots show the center line as the median, whiskers show the maxima and minima, and box limits show upper and lower quartiles.

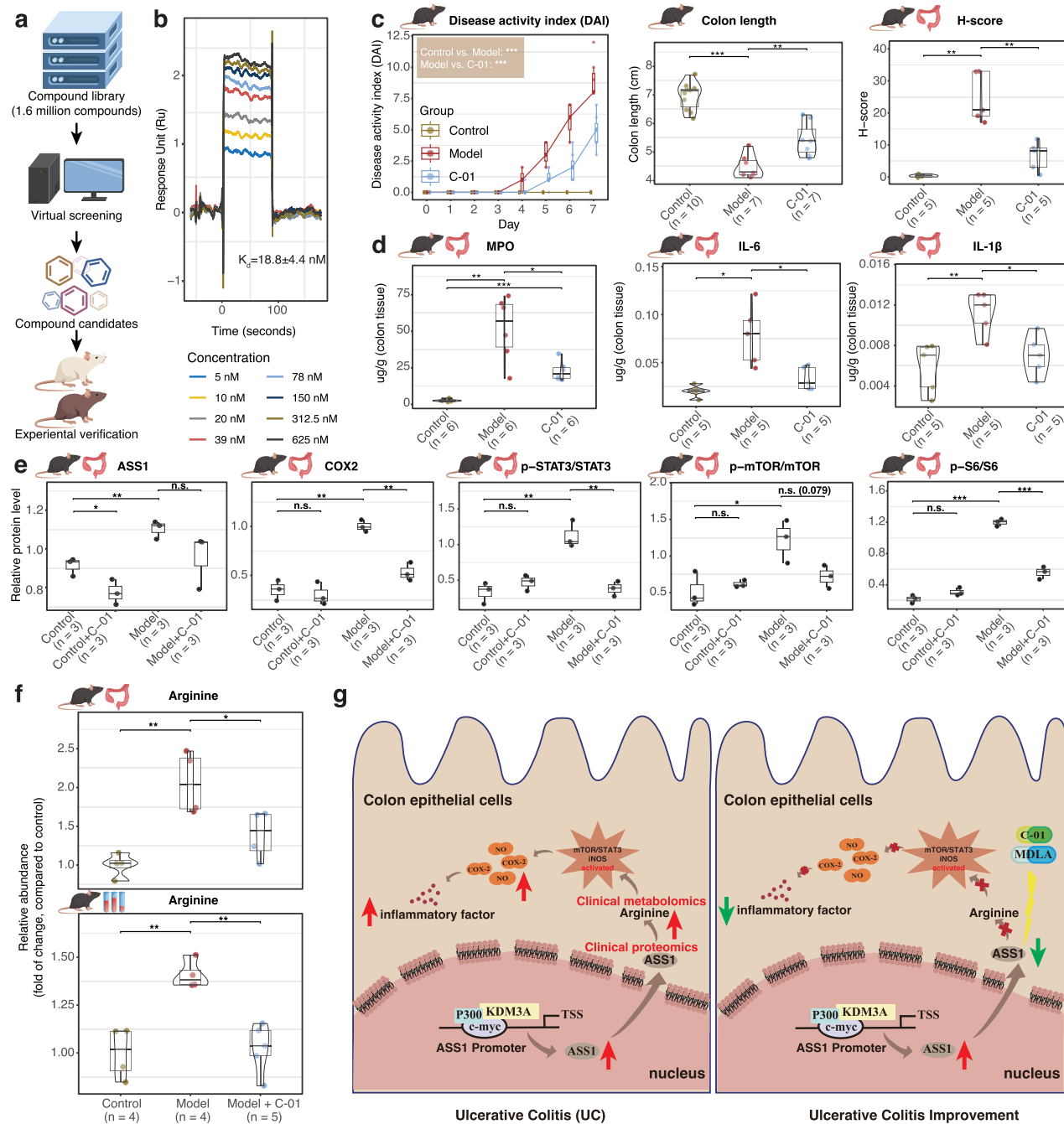


Fig. 7 | Screening identifies C-01 as an inhibitor of ASS1. **a** A Workflow for the screening, identification, and experimental verification of ASS1 inhibitors. **b** The binding ability of C-01 to ASS1 tested by surface plasmon resonance (SPR) ($n=3$). **c** C-01 supplementation alleviates clinical outcomes in UC mouse models. Disease activity index (DAI): Control vs Model ($p=1.73e-13$), Model vs C-01 ($p=2.92e-06$); Colon length: Control vs Model ($p=1.12e-08$), Model vs C-01 ($p=0.005$). H-score: Control vs Model ($p=0.002$), Model vs C-01 ($p=0.003$). Disease activity index was analyzed using repeated measures ANOVA; colon length and H-score were compared using Welch's t test. ($n=10$ for Control, $n=7$ for Model and $n=7$ for C-01 in DAI score and colon length). **d** C-01 significantly decreases myeloperoxidase activity and proinflammatory cytokines (IL-6 and IL-1 β) in the colon tissues of UC mouse models. MPO: Control vs Model ($p=0.003$), Control vs C-01 ($p=0.0006$), Model vs C-01 ($p=0.02$). IL-6: Control vs Model ($p=0.01$), Model vs C-01 ($p=0.03$). IL-1 β : Control vs Model ($p=0.006$), Model vs C-01 ($p=0.01$). Comparisons were performed using Welch's t test. **e** C-01 supplementation significantly inhibits the mTOR signaling pathway in UC mouse models (colon tissues). ASS1: Control vs Control + C-01 ($p=0.048$), Model vs Model + C-01 ($p=0.204$), Control vs Model

($p=0.008$); COX2: Control vs Control + C-01 ($p=0.630$), Model vs Model + C-01 ($p=0.003$), Control vs Model ($p=0.002$); p-STAT3/STAT3: Control vs Control + C-01 ($p=0.271$), Model vs Model + C-01 ($p=0.009$), Control vs Model ($p=0.006$); p-mTOR/mTOR: Control vs Control + C-01 ($p=0.549$), Model vs Model + C-01 ($p=0.079$), Control vs Model ($p=0.035$); p-S6/S6: Control vs Control + C-01 ($p=0.088$), Model vs Model + C-01 ($p=0.00008$), Control vs Model ($p=0.00002$). Statistical significance was determined using Welch's t test. **f** C-01 significantly decreases arginine levels in the colon tissue and blood of UC mouse models. Colon tissue arginine: Control vs DSS ($p=0.009$), DSS vs C-01 ($p=0.043$). Blood arginine: Control vs DSS ($p=0.004$), DSS vs C-01 ($p=0.001$). Comparisons were performed using Welch's t test. **g** Proposed mechanism illustrating how ASS1 blockade by C-01 alleviates intestinal inflammation in UC. Box plots show the center line as the median, whiskers show maxima and minima, and box limits show upper and lower quartiles. UC, ulcerative colitis; MPO, myeloperoxidase; IL-6, Interleukin-6; IL-1 β , Interleukin 1 β ; mTOR, mammalian target of rapamycin; STAT3, signal transducer and activator of transcription 3; S6, Ribosomal protein S6; COX-2, Cyclooxygenase-2; H score, Histological score; ASS1, argininosuccinate synthetase 1.

To predict the binding mode of C-01 with ASS1, three 400-ns MD simulations were performed independently. According to the RMSD of the protein backbone atoms and C-01 during the MD simulation (Supplementary Fig. 29a), the complex achieved equilibrium after 140 ns, and then the representative conformation was extracted. As shown in Supplementary Fig. 29b, C-01 occupied the orthosteric sites of ASS1 and formed five hydrogen bonds with Arg157, Lys176, Met181, and Arg272 of ASS1, respectively. Correspondingly, the binding energy calculated through the Molecular Mechanics-Poisson Boltzmann Surface Area (MM-PBSA) method was -32.02 ± 1.26 kcal·mol⁻¹, suggesting a potent interaction; meanwhile, energy decomposition on residues showed that Arg157 and Lys176 made stronger contributions. Thereafter, a surface plasmon resonance (SPR) assay was implemented to measure the binding ability of the compound with human recombinant ASS1, in which C-01 showed a strong binding affinity with an estimated equilibrium dissociation constant (K_d) of 18.8 ± 4.4 nM (Fig. 7b). These results indicated that C-01 could bind to ASS1 directly and potently.

Next, we investigated the potential effects of C-01 on the development of colonic inflammation at the animal level. Treatment with C-01 effectively lowered DAI scores, alleviated colon shortening, ameliorated colonic histopathology, and reduced the levels of proinflammatory cytokines in mice with colitis (Fig. 7c, d). Chronic infusion of C-01 did not affect the histopathology of the colon in control mice (Supplementary Fig. 11c). Further exploration found that the upregulated protein level of COX-2, P-mTOR, P-STAT3 and P-S6 in DSS mice were suppressed by C-01 treatment (Fig. 7e). In addition, downregulation of arginine levels in both colon tissue and blood was observed in C-01-treated mice (Fig. 7f).

For the pharmacokinetics study, we found the $T_{1/2z}$ value was about 252 min, C_{max} was 9.34 μg/mL, AUC was about 971 μg·mL⁻¹·mL, and CL was about 12 mL/min/Kg in rat plasma after oral administration of 10 mg/kg C-01 (Supplementary Table 16). For the colonic tissue distribution study, we found the achievable and sustainable concentration of C-01 in colonic tissue reached micromole in mice, which aligns with the efficacy concentration in cells (Supplementary Fig. 30a). Therefore, these pharmacokinetic parameters were within an acceptable range and indicated that C-01, with good pharmacokinetic characteristics, was a potential drug candidate for UC treatment. Importantly, a single administration of C-01 (200 mg/kg) had no effect on the body weight and histological features of the heart, liver, spleen, lungs, and kidneys of mice (Supplementary Fig. 30b, c). We have provided credible evidence in support of the fact that C-01 could hold great promise in ameliorating colitis.

Discussion

Emerging evidence suggests that the pathogenesis of UC is intimately related to alterations in bioactive metabolites derived from the host and/or gut microbiota, such as lipid and amino acid metabolites³⁴. These metabolites, such as trimethylamine N-oxide (TMAO), might play essential roles in the etiology of UC by modulating cellular signal transduction and immune responses³⁵. Nonetheless, the importance of metabolites in the pathogenesis of UC remains underappreciated due to the complexity of metabolites and metabolic pathways. In the present study, we used multi-omics data (metabolomics and proteomics) to reveal that ASS1 and its metabolite arginine were elevated in both UC patients and UC mouse models. Higher serum arginine levels are positively associated with disease severity in UC patients, suggesting that arginine might have tremendous potential as a biomarker to assess disease severity in UC. Exogenous arginine infusion and overexpression of ASS1 deteriorated DSS-induced colitis. Conversely, blockade of arginine or gene ablation of ASS1 significantly decreased colonic inflammation and the histopathological score. Mechanistically, ASS1-derived arginine induced mTOR/STAT3 over-activation and COX-2 upregulation, thus leading to an inflammatory storm in colonic tissue

(Fig. 7g). Also, we unveiled an epigenetic mechanism whereby histone-modifying enzymes mediated transcriptional activation of ASS1 during the development of UC. Notably, we screened C-01 from 1.6 million libraries, and this compound had a good affinity for ASS1 and significantly recovered DSS-induced colitis in mice. This study provides insights into the ASS1/Arginine Axis in UC pathogenesis and opens up a field of UC prevention and treatment. We also provided robust evidence in support of the fact that ASS1-targeted C-01 may be an attractive therapeutic drug for UC.

mTOR, an evolutionarily conserved serine/threonine protein kinase, integrates various environmental signals into cellular metabolism to maintain cellular homeostasis³⁶. This kinase exists as the catalytic subunit of two functionally distinct signaling complexes, mTOR complex 1 (mTORC1) and mTORC2³⁷. Classically, mTOR serves as a master regulator of cell growth in response to nutrient supply and growth factors. Aside from its crucial role in tumorigenesis, recent studies have shown that mTOR activation is involved in diverse inflammatory diseases, including UC³⁸. Specifically, activated mTOR is observed in colon biopsies of DSS-induced colitis mice³⁹. Inactivation of mTOR is sufficient to attenuate colitis in DSS-induced mice or interleukin-10 (IL-10) knockout mice^{38,40,41}. Phosphorylated mTOR promotes the synthesis of IL-17 by regulating the STAT3, HIF-1α, S6K1, and S6K2 pathways⁴², and overproduction of IL-17 is associated with the occurrence and development of numerous autoimmune diseases, such as UC^{43,44}. mTOR contributes to the activation of STAT3 by STAT3 phosphorylation, which is involved in DSS-induced colitis in mice^{45,46}. Also, colonic epithelial mTORC1 activates COX-2 transcription via inducing STAT3 phosphorylation and enhancing its binding to the COX-2 promoter, leading to Th17 cell infiltration in the colon and UC development in mice⁴⁴. In addition, arginine is a direct activator of mTOR, and its depletion is a therapeutic strategy for carcinogenesis²⁴. Dietary arginine supplementation activates intestinal innate immunity and initiates the expression of proinflammatory cytokines and secretory immunoglobulin A in the jejunum and ileum⁴⁷. Altogether, the Arginine-mTOR axis might hold broad therapeutic implications for inflammatory diseases, such as UC. Metabolic pathway enrichment analysis showed that the mTOR pathway was activated in UC patients, suggesting that arginine might act on the mTOR pathway to be involved in the pathological process of UC. To resolve this hypothesis, we examined the effects of arginine infusion or inhibition on the occurrence and development of UC in vitro and in vivo. As expected, pretreatment with arginine aggravated IL-6-induced phosphorylation levels of mTOR, STAT3, S6, and COX-2, as well as the inflammatory factor IL-1β in colon epithelial cells. In keeping with the cellular results, chronic administration of arginine accelerated the development of DSS-induced colitis in mice, with concomitant increases in the protein levels of P-mTOR, P-STAT3, P-S6, COX-2, and inflammatory cytokine release. On the contrary, inhibition of arginine by MDLA^{31,32,48}, an inhibitor of ASS1 that contributed to the generation of arginine, displayed the opposite effects. These results prove that arginine may drive the onset and development of DSS-induced colitis by overactivating the mTOR pathway and its downstream proteins.

Arginine is considered a non- or semi-essential amino acid since normal cells have the intrinsic ability to regulate endogenous arginine via ASS1 and ASL in the urea cycle⁴⁹. Specifically, ASS1 catalyzes the condensation of citrulline and aspartate to give rise to argininosuccinate, and this immediate precursor is then converted to arginine with the aid of ASL⁵⁰. Coincidentally, a recent bioinformatics analysis identifies ASS1 as a candidate diagnostic biomarker for UC⁵¹. Based on this, it is intriguing to know whether these two enzymes involved in arginine production played a role in the pathogenesis of UC. Our results showed that the transcriptional and translation levels of ASS1 were dramatically upregulated in UC patients, indicating that ASS1 might be responsible for the overproduction of arginine in UC patients. We next determined the significance of ASS1 in the

pathogenesis of UC. We found that overexpression of ASS1 led to arginine overproduction and aggravated the pathological process of colitis by activating the mTOR pathway *in vitro* and *in vivo*. By contrast, ASS1 deficiency resulted in arginine depletion and ameliorated the development of colitis by inactivating the mTOR pathway.

In addition, we showed that there was a simultaneous upregulation of both acetylated H3 and trimethylated H3K4 and downregulation of dimethyl H3K9 around the proximal ASS1 promoter in IL-6-treated cells, suggestive of transcriptional activation of ASS1 in UC. Previously, the constitutive binding of the transcription factor c-Myc to the ASS1 promoter led to elevated ASS1 expression in melanoma cells^{52,53}. Induction of ASS1 is mediated by activation of c-Myc in breast cancer under glucose deprivation conditions³². The histone acetyltransferase p300 is normally associated with the ASS1 promoter⁵⁴, indicating that p300-mediated chromatin remodeling governs the transcription of ASS1. KDM3A, a demethylase of histone H3K9me1/2, is associated with p300 and required for p300 recruitment to enhancers of hippo target genes⁵⁵.

Moreover, upregulation of KDM3A is correlated with poor prognosis of colon carcinogenesis⁵⁶. These findings propel us to examine whether c-Myc drives the transcriptional activation of ASS1 in colitis by recruiting the acetyltransferase p300 and the H3K9 demethylase KDM3A. Our results showed that c-Myc might contribute to ASS1 transactivation by sequentially recruiting p300 and KDM3A to the ASS1 promoter. Our results demonstrated that histone acetylation mediated colitis-induced ASS1 overexpression, thus leading to arginine overproduction and subsequent colitis development. Eventually, we screened 1.6 million bioactive compounds for candidate inhibitors of ASS1 and found that C-01 supplementation improved colonic inflammation in DSS-induced colitis mice, similar to the anti-inflammatory effects of C-01 on NCM460 cells exposed to IL-6. These findings suggest that the ASS1/Arginine axis might serve as a target for clinical intervention in UC patients.

Arginase 1 (Arg1), an enzyme that converts L-arginine into ornithine and urea, is upregulated in intestinal tissues from IBD patients, and Arg1 deletion promotes the resolution of colitis in a mouse model of IBD, indicating that arginine metabolism may be highlighted as a pathway for the intervention of IBD⁵⁷. Inhibition of arginase might effectively alleviate the pathogenesis of colonic inflammation⁵⁸. ASL is an enzyme that produces arginine, the substrate for NO generation by nitric oxide synthase (NOS) isoforms, and ASL-mediated NO production in enterocytes alleviates colitis by mitigating macrophage infiltration and tissue damage⁵⁹. Notably, ASL-mediated NO formation in immune cells increases the severity of colonic inflammation and inflammation-associated colon cancer via macrophage activation⁵⁹. ASS1 protein is abundantly expressed in the immune system, including the thymus and T cells from human and mouse tissues⁶⁰. Importantly, ASS1 deficiency results in T-cell defects and primary immune dysfunction⁶⁰. Moreover, hepatocyte-intrinsic IFNAR1 suppressed the transcription of metabolic genes, including Otc and ASS1, that led to decreased arginine and increased ornithine concentrations in the circulation, suppressed virus-specific CD8+ T cell responses, and improved liver pathology⁶¹. Upregulation of ASS1 is required for efficient proinflammatory signaling activation in macrophages, and blockage of ASS1 suppresses the host defense against bacterial infection⁶². These findings indicate that ASL and ASS1, two major enzymes for arginine production, might play an important role in regulating inflammatory response via a tissue- or cell-specific manner. As such, the function roles of ASL and ASS1 in the pathogenesis of colonic inflammation merit further studies using cell-specific ASS1 knockout mice, including colon epithelial cells, macrophages, and T cells.

Given that arginine is a natural agonist of mTOR, arginine may be a driver for the development and progression of UC. However, the effects of arginine on UC pathogenesis may be inconsistent. Consistent

with our results, serum arginine levels are obviously augmented in subjects with colitis compared to normal controls, and there is a strong correlation between the Mayo Disease Activity Index (DAI) and serum arginine levels⁶³. Arginine levels are upregulated in active-UC patients and DSS-induced mice^{64,65}. Yet, a previous study found that serum arginine levels were not different between 137 UC patients and 38 healthy controls⁶⁶. In this study, the authors also found that the arginine levels in the colon tissues decreased in patients with active UC⁶⁶.

It has been reviewed that arginine metabolism is closely associated with the pathogenesis of IBD⁶⁷. They concluded that the dosage of arginine may need to be carefully tailored for different individuals at different disease stages⁶⁷. Moreover, it was reported that colon arginine levels and the arginine availability index were inversely correlated with disease activity indices in UC patients⁶⁶. These findings collectively supported a pattern of dysregulated arginine availability and metabolism in UC patients. However, inconsistent results of arginine levels in circulation and colon from UC patients were reported. Therefore, a large-scale clinical study is highly recommended to determine the actual concentrations of arginine in both the circulation and colon tissues of UC patients using more sensitive and accurate inspection methods. Moreover, dietary intake of arginine at very high doses improves body weight loss, colon length shortening, and histological injury in the dextran sulfate sodium (DSS) model of colitis^{68–70}. It is worth mentioning that in the same study, low arginine concentrations did not ameliorate DSS-induced colitis in mice, while a high dose of arginine was protective in colitis models⁶⁸. In the meantime, administration of arginine increases the formation of nitrotyrosine and causes mucosal damage in collagenous colitis⁷¹. These inconsistent results propelled us to delineate the exact roles and underlying mechanisms of arginine in the pathogenesis of UC, which might lead to treatment options derived from the arginine pathway. Very recently, arginine restriction or deprivation could induce cancer cell apoptosis and tumor regression^{72,73}, highlighting the pathologic role of arginine accumulation in cancer progression. It has been demonstrated that arginine/NO derived from enterocytes alleviates colitis by decreasing macrophage infiltration and tissue damage, whereas immune cell-derived arginine/NO is associated with macrophage activation, resulting in increased severity of inflammation⁵⁹. Moreover, arginine can simultaneously modify mammalian immune functions, intraluminal metabolism, intestinal microbiota, and microbial pathogenesis⁷⁴. Based on the role of arginine in UC from previous findings and our own results, we deduced that low-dose arginine is pathogenic, while high-dose arginine is protective in UC, forming a parabolic dose relationship. The apparent inconsistency in the effects of low-dose versus high-dose arginine in UC could be attributed to several factors, including dosage-dependent biochemical pathways, immune modulation, metabolic regulation, and tissue-specific effects. This dysregulated arginine availability in the colon is closely linked to disease severity, possibly due to impaired absorption or increased consumption of arginine by activated immune cells and epithelial cells during inflammation. In this context, the paradoxical effects of arginine supplementation in UC could be explained by the stage of disease, tissue-specific effects, and individual variability in arginine metabolism. A key observation from recent studies and our own results is the suggestion of a parabolic dose-response relationship for arginine in UC. This hypothesis proposes that low doses of arginine may exacerbate disease through increased production of nitrotyrosine, a marker of oxidative stress and tissue damage in colitis models. This could occur due to the increased formation of reactive nitrogen species (RNS), which leads to nitrosative stress, promoting further inflammation and mucosal damage in UC. On the other hand, high doses of arginine are thought to have a protective effect, improving disease outcomes such as body weight loss, colon length shortening, and histological injury in DSS-induced colitis. This protective effect is likely mediated by the conversion of arginine to nitric oxide (NO) by nitric

oxide synthase (NOS), which has anti-inflammatory and tissue-protective properties. This tissue-specific differentiation is crucial when considering the paradox of arginine supplementation in UC. The different effects of arginine in epithelial cells and immune cells could explain why low-dose arginine might increase inflammatory markers, while high-dose arginine could improve mucosal healing and reduce inflammation through epithelial-derived NO.

In immune cells, particularly macrophages and T cells, ASS1 modulates arginine flux, which can influence inflammatory pathways⁷⁵. Pro-inflammatory macrophages (M1) use arginine to produce NO and reactive nitrogen species, while anti-inflammatory macrophages (M2) may utilize arginine for polyamine synthesis, promoting tissue repair⁷⁶. ASS1 inhibition in immune cells might shift the balance between pro- and anti-inflammatory phenotypes, potentially affecting the overall inflammatory response in UC. To address this complexity, future studies should utilize cell-specific knockout models. These models can clarify the distinct contributions of ASS1 in epithelial cells versus immune cells, particularly under inflammatory and regenerative conditions. Investigating how ASS1 modulates metabolic flux in different cell types will provide deeper insights. Furthermore, arginine metabolism is also closely linked to the intestinal microbiota⁷⁴. The microbiota can influence the bioavailability of arginine and its downstream metabolic products. Dysbiosis, often seen in UC, could further contribute to the inconsistent effects of arginine, potentially altering its role in gut inflammation based on the microbial composition in different individuals. Future studies, both preclinical and clinical, are required to better define the optimal dosing of arginine in UC patients, accounting for individual variability, disease stage, and potential microbiota interactions. A large-scale clinical trial with more sensitive and accurate techniques will be essential to establish precise arginine concentrations in circulation and colonic tissues, helping to guide therapeutic interventions in UC.

The present study is subject to certain constraints. Intestinal epithelial cell-specific ASS1 knockout mice should be used to further clarify the role of ASS1 in the development of UC. IL-6 is a key cytokine implicated in UC pathogenesis due to its role in promoting inflammation, IEC dysfunction, and immune dysregulation. While IL-6 treatment provides a simplified approach to model aspects of the inflammatory state seen in UC, we recognize that it does not fully replicate the multifactorial nature of UC, which involves a complex interplay of immune cells, microbial dysbiosis, and additional inflammatory mediators. Cytokines such as TNF- α , IL-1 β , and IL-17, as well as microbial metabolites, are crucial components of UC pathophysiology. Future studies could incorporate multi-cytokine treatments or co-culture systems involving immune cells to better mimic the UC environment. Although DSS-induced colitis is widely used, it may not fully represent the complexity of UC in humans. For example, it lacks the adaptive immune component seen in chronic colitis. Combining DSS with genetic models (e.g., IL-10 KO mice) or using humanized mouse models could improve translational relevance. The study suggests a parabolic dose-response relationship for arginine in UC. However, only acute DSS models were used, which may not fully capture the long-term effects of arginine supplementation or inhibition. Chronic colitis models could provide insights into the role of arginine across different disease stages. ASS1 and arginine metabolism may have cell-type-specific effects in UC, as suggested by the dual roles of arginine in epithelial and immune cells. Conditional knockout models targeting ASS1 in specific cell types, such as epithelial cells or macrophages, would help clarify these tissue-specific contributions. The study does not address potential sex-based differences in arginine metabolism and ASS1 expression. Given that UC may present differently between males and females, stratifying data by sex could uncover important nuances. Of note, AAVs have demonstrated the greatest clinical success in hepatic systems, as highlighted in recent reviews⁷⁷. While enema-mediated delivery of AAV vectors has shown promise for

targeted gene modulation in the colonic epithelium, several important questions remain to be addressed in future studies to fully harness its therapeutic potential. First, systematic optimization of vector design, including capsid serotype, genome configuration, and promoter selection, will be essential to enhance transduction efficiency, tissue specificity, and duration of expression across different epithelial and immune cell populations within the colon. Second, cell-type-specific tropism and penetration depth remain underexplored. Third, the durability and safety of transgene expression following enema administration require long-term follow-up, particularly in the context of chronic diseases like ulcerative colitis or colorectal cancer. With continued advances in vector engineering, delivery techniques, and translational models, this strategy has the potential to open frontiers in treating mucosal diseases with precision.

Altogether, our results redefine the role of ASS1/Arginine in UC pathology and the duality of arginine in the development of UC. Overexpression of ASS1 or a low dose of arginine might facilitate the development of UC by activating the mTOR pathway. We expect that this study will provide a rationale for clinical studies of arginine in UC and call the attention of researchers to the dual role of arginine in the pathogenesis of UC. Therapeutic targeting of ASS1 by C-01 might be a valuable candidate for managing UC, and its clinical translation awaits further research. Further studies are needed to fully validate the target ASS1 and characterize the drug candidate C-01.

Methods

Recruitment of patients with UC and normal participants

All procedures were approved by the medical ethics committee of the Affiliated Hospital of Nanjing University of Chinese Medicine and followed the tenets of the Declaration of Helsinki. All participants were recruited during their visits to the hospital for medical examinations or doctor consultations. The patients were diagnosed according to the American College of Gastroenterology clinical guideline for UC. Patients with kidney injury, liver disease, active vasculitis, other gastrointestinal pathology, or cancer, etc. were excluded from the study. All participants were informed of using blood or colonic mucosal biopsy samples, and written informed consent was obtained. Sera from 131 UC patients and 127 age- and sex-matched healthy subjects as metabolic discovery sets were collected from the Department of Gastroenterology, the Affiliated Hospital of Nanjing University of Chinese Medicine (Supplementary Table 1). Sera from 141 UC patients and 136 age- and sex-matched healthy subjects as metabolic validation set 1 were collected from the Department of Gastroenterology, the Affiliated Hospital of Nanjing University of Chinese Medicine (Supplementary Table 6). Sera from 30 UC patients and 30 age- and sex-matched healthy subjects as metabolic validation set 2 were collected from the Nanjing Hospital of Chinese Medicine, Affiliated to the Nanjing University of Chinese Medicine (Supplementary Table 7). Sera from 30 UC patients and 30 age- and sex-matched healthy subjects as metabolic validation set 3 were collected from the Affiliated Jiangyin Hospital of Nanjing University of Chinese Medicine (Supplementary Table 8). Faecal samples from UC patients and age- and sex-matched healthy subjects were collected from the Affiliated Hospital of Nanjing University of Chinese Medicine (Supplementary Table 9). Sera from UC patients and age- and sex-matched healthy subjects for determination of argininosuccinate, ornithine, NO, and urea were collected from the Affiliated Hospital of Nanjing University of Chinese Medicine (Supplementary Table 10). Inflamed and normal colonic mucosal biopsies using label-free proteomics were collected from the Department of Gastroenterology, the Affiliated Jiangyin Hospital of Nanjing University of Chinese Medicine (Supplementary Table 11). The Western blot and mRNA levels of ASS1 and ASL were determined in UC patients from the Affiliated Jiangyin Hospital of Nanjing University of Chinese Medicine (Supplementary Table 12). The colon slices of UC patients and healthy participants for histology analysis of ASS1 were also collected from the

Department of Gastroenterology, the Affiliated Hospital of Nanjing University of Chinese Medicine (Supplementary Tables 13 and 14).

The comparison of vegetable and meat intake was evaluated using the chi-squared test, showing no significant differences across all human cohorts. For the discovery cohort, the *p*-value for vegetables is 0.992, and for meat, it's also 0.992. In validation cohort 1, the *p*-value for vegetables is 0.999, compared to 0.9992 for meat. In validation cohort 2, the *p*-value for vegetables is 0.9908, while for meat, it is 0.9987. In validation cohort 3, the *p*-value for vegetables is 0.9816, and for meat, it is 0.9975.

DSS-induced colitis in mice

Female C57BL/6J mice, aged 8–10 weeks, were purchased from the GemPharmatech Co., Ltd. (Nanjing, China). Upon arrival, the mice were maintained with free access to protein-bound arginine chow and water in plastic cages at $20 \pm 2^\circ\text{C}$ and kept on a 12 h light-dark cycle. The mice were allowed to acclimate to their environment for 1 week before any experimental procedures. All animal experiments were approved by the Ethics Committee of Nanjing University of Chinese Medicine and were conducted in accordance with institutional guidelines for animal welfare and ethical standards. For the induction of acute colitis, mice were orally administered L-arginine (Shanghai Yuanye Bio-Technology Co., Ltd., China. Lot No. S20008, purity: 98%) at a dose of 200 mg/kg body weight. At the same time, they were given 3.5% dextran sulfate sodium (DSS, MP Biomedicals) in their drinking water ad libitum for a period of 6 days. DSS was dissolved in filtered tap water, and the mice were monitored daily for signs of colitis, such as body weight loss, diarrhea, and rectal bleeding. To evaluate the effect of ASS1 inhibition on colitis development, mice were orally administered with ASS1 inhibitor α -Methyl-DL-aspartic acid (MDLA, CSNPharm. Catalog No. CSN83915, purity: 98%) at a dose of 100 mg/kg. Simultaneously, they were provided with 3.5% DSS in their drinking water for seven consecutive days. The MDLA was dissolved in sterile saline and administered daily via oral gavage. To evaluate the effects of ASS1 downregulation on the development of colitis, mice were subjected to enema injection with either AAV9 vectors carrying short hairpin RNA (shRNA) targeting ASS1 (target sequence: 5'-CCTCATG-CACATCAGCTAT-3') or AAV9 vectors carrying full-length cDNA of human ASS1 (AAV9-ASS1). The AAV9 vectors were purchased from Hanbio Biotechnology Co., Ltd. (Shanghai, China). Each mouse was administered a 150 μL dose of AAV9 solution (2×10^{12} vg/mL) in every two weeks (0, 2, and 4th week) by enema injection. After the gene modulation treatment for 5 weeks, mice were exposed to DSS for 7 days to induce colitis. The ASS1 overexpression (OE) group was treated with 3% DSS in drinking water, whereas the ASS1 knockdown (shRNA) group received 3.5% DSS. To evaluate the role of nitric oxide (NO) synthases in the development of colitis, mice were treated with specific inhibitors of inducible nitric oxide synthase (iNOS) and endothelial nitric oxide synthase (eNOS). The iNOS inhibitor, 1400 W dihydrochloride (Shanghai Yuanye Bio-Technology Co., Ltd., China. Lot No. S81435, purity: 98%), was administered orally at a dose of 20 mg/kg body weight. The eNOS inhibitor, carboxyebselein (Target Mol), was also administered orally at a dose of 20 mg/kg body weight. These inhibitors were given once daily for the duration of the experiment. At the end of the experiment, the mice were anesthetized using isoflurane (3% induction and 1.5% maintenance) to minimize suffering. Blood was collected via cardiac puncture from the right ventricle of the heart into non-heparinized tubes, and serum was obtained after centrifugation at $1000 \times g$ for 10 min at 4°C . For histopathological analysis, a portion of the colon was immediately excised and fixed in 4% paraformaldehyde (PFA) for 24 h. The fixed tissue was then embedded in paraffin and sectioned at 4 μm thickness for subsequent histological staining. The remaining colon tissue samples were snap-frozen in liquid nitrogen and stored at -80°C until further biochemical or molecular analysis.

Cell culture and drug treatment

NCM460 cells were used for in vitro experiments, and these cells were maintained in Dulbecco's Modified Eagle Medium (DMEM, C3113-0500, VivaCell) supplemented with 10% fetal bovine serum (FBS, Gibco, Catalog No. 16000-044) and 1% penicillin-streptomycin (Pen/Strep, NCM Biotech, Catalog No. C100CS). NCM460 cells were cultured at 37°C in a humidified incubator with a 5% CO₂ atmosphere. The culture medium was replaced every 2–3 days to maintain cell viability. To simulate an inflammatory environment, NCM460 cells were treated with recombinant human interleukin-6 (IL-6, R&D Systems, USA). IL-6 was reconstituted according to the manufacturer's instructions. Cells were treated with 10 ng/mL of recombinant human IL-6 for a duration of 24 h to induce inflammation and study its effects on the cells. For the assessment of the effects of arginine and its inhibition, arginine (200 μM) and MDLA (50 μM) were used in the experiments. These compounds were dissolved in the culture medium and freshly prepared prior to each treatment. Arginine (Sigma-Aldrich or another supplier) was used at a concentration of 200 μM to assess its effects on cell viability, cytokine production, and potential modulation of inflammatory pathways in the context of IL-6 treatment. MDLA (α -Methyl-DL-aspartic acid, CSNPharm, Catalog No. CSN83915) was used as an ASS1 inhibitor at a concentration of 50 μM . MDLA was added to the culture medium simultaneously with IL-6 treatment, and cells were treated for 24 h. NCM460 cells were seeded in 6-well plates or appropriate culture vessels (depending on the assay to be performed) and allowed to adhere for 24 h. After cell attachment, cells were concurrently treated with 200 μM arginine or 50 μM MDLA for 24 h. After that, the cells were then stimulated and treated with recombinant human IL-6 (10 ng/mL) for an additional 24 h. After the 24 h treatment period, cells were harvested for downstream assays, including cell viability assays, gene expression analysis, protein extraction, and cytokine measurement.

Primary cell culture

The isolation of primary intestinal epithelial cells was performed as depicted previously^{78–80}. In short, the colon was removed from the sacrificed mice, longitudinally opened, and washed with sterile ice-cold PBS to remove all fecal material. The colon was cut into 1 cm pieces and treated with ice-cold 8 mM EDTA/PBS, containing 1% pen-strep for 1 h at 4°C . After that, the tissues were incubated with collagenase (2 mg/mL) and gentamycin (50 $\mu\text{g}/\text{mL}$) in F12-DMEM supplemented with 10% FBS, 1% Glutamax, and 1% pen-strep for 10 min at 37°C . Crypts were subsequently dissociated by 30 s vortexing and repeating the process 5 times. The isolated crypts were then collected through centrifugation at $1000 \times g$ for 5 min at 4°C . Primary intestinal epithelial cells were further purified through density gradient centrifugation with 20% and 40% Percoll-RPMI solution. Finally, the cells were cultured in 6-well plates following Matrigel embedding and then subjected to further experiments.

Lentiviral cell transfection

To establish stable cell lines with ASS1 knockdown or overexpression, lentiviral vectors were used. These vectors were provided by Hanbio Biotechnology Co., Ltd. (Shanghai, China). A lentiviral vector carrying the ASS1-shRNA (ASS1 shRNA sequence: 5'-GCCTGAATTCTAACCGGTT-3'.HBLV-h-ASS1-3xflag-EF1-ZsGreen-PURO) was used to knock down ASS1 expression. The vector expresses green fluorescent protein (GFP) and puromycin resistance for selection. A lentiviral vector encoding the ASS1 gene (HBLV-h-ASS1-3xflag-EF1-ZsGreen-PURO) was used to induce overexpression of ASS1 in NCM460 cells. The negative control vector (HBLV-ZsGreen-PURO) expresses GFP and puromycin resistance, but does not target ASS1, and was used as a control. In brief, lentiviral vectors were produced by transfecting HEK293T cells with the lentiviral plasmids (ASS1 knockdown or overexpression) along with the packaging plasmids, following the

manufacturer's protocol. The virus-containing supernatant was collected after 48 h and filtered through a 0.45 µm filter to remove cellular debris. NCM460 cells were seeded in 6-well plates or appropriate culture vessels, and lentivirus was added to the cells at a multiplicity of infection (MOI) of 20. The viral supernatant was mixed with fresh culture medium, and polybrene (Sigma-Aldrich) was added to a final concentration of 8 µg/mL to enhance transduction efficiency. The cells were incubated with lentivirus for 24 h at 37 °C, with the viral solution replaced by fresh medium after 24 h. After viral transduction, stable cell lines were selected using puromycin. NCM460 cells were treated with 3 µg/mL puromycin for 14 days to select for cells that had successfully integrated the lentiviral vectors expressing puromycin resistance. The medium was replaced every 2-3 days, and dead cells were removed by gentle washing with PBS. Surviving colonies were allowed to expand. After 14 days of puromycin selection, cells were harvested and lysed using RIPA buffer (with protease inhibitors) for protein extraction. The protein concentration was measured using the BCA assay (Pierce). Equal amounts of protein (30–50 µg) were separated by SDS-PAGE and transferred to PVDF membranes. Membranes were probed with primary antibodies against ASS1.

Western blot

The tissues and cells were harvested and then lysed in RIPA buffer (Sigma-Aldrich, Catalog No. R0278) containing protease inhibitors (Sigma-Aldrich, Catalog No. P8340) and phosphatase inhibitors (Sigma-Aldrich, Catalog No. 4906845001) to prevent protein degradation and dephosphorylation. The lysates were incubated on ice for 30 min with periodic vortexing. Cell debris was removed by centrifugation at 12,000 × g for 10 min at 4 °C. The supernatant (containing the protein extract) was collected and stored at –80 °C until use. The protein concentration of the lysates was determined using the BCA Protein Assay Kit (Pierce, Catalog No. 23225) according to the manufacturer's protocol. Equal amounts of protein (30 µg) were mixed with 4× Laemmli Sample Buffer (Sigma-Aldrich, Catalog No. S3401) containing DTT (Sigma-Aldrich, Catalog No. D0632) as a reducing agent. The samples were then heated at 95 °C for 5 min to denature the proteins. Proteins were separated by Sodium Dodecyl Sulfate-Polyacrylamide Gel Electrophoresis (SDS-PAGE) using a 10–12% polyacrylamide gel (depending on the size of the target protein). The proteins were transferred onto a polyvinylidene fluoride (PVDF) membrane (Bio-Rad, Catalog No. 1620177) using a wet transfer system (Bio-Rad) at 100 V for 1 h in transfer buffer (25 mM Tris, 192 mM glycine, 20% methanol). The PVDF membrane was blocked with 5% non-fat dry milk (or 5% bovine serum albumin (BSA) for phospho-protein blots) in Tris-buffered saline with Tween-20 (TBST) (20 mM Tris, 150 mM NaCl, 0.1% Tween-20, pH 7.4) for one h at room temperature to prevent non-specific binding. The membrane was incubated with the following primary antibodies: anti-ASS1 antibody (16210-1-AP, Proteintech), anti-COX-2 antibody (I2282, CST), anti-S6 antibody (2317, CST), anti-p-S6 antibody (4858, CST), anti-STAT3 antibody (4904, CST), anti-p-STAT3 antibody (9134, CST), anti-mTOR antibody (66889-1-Ig, Proteintech), anti-p-mTOR antibody (5536, CST), anti-ASL antibody (16645-1-AP, Proteintech), anti-IL1β antibody (66737-1-Ig, Proteintech) anti-GAPDH monoclonal antibody (IHRP-60004, Proteintech), HRP-linked anti-rabbit IgG (SA00001-2, Proteintech), HRP-linked anti-mouse IgG (SA00001-1, Proteintech). Semi-quantitative analysis of each protein was performed using ImageJ software (version 1.5), and the band densities were normalized to the band density of GAPDH.

Histology analysis and immunohistochemistry

After sacrificing the mice, the colonic tissues were collected from individual mice in each treatment group and immediately fixed in 4% paraformaldehyde. Paraffin sections (5 µm) of colonic tissues were prepared and stained with H&E histological staining. The colon

(number of lesions) pathology was quantified according to the mucosal ulcer, recess destruction, inflammatory cell infiltration, inflammatory exudate, and fibrosis by the same pathological person⁸¹. Deparaffinized colon sections in each group were subjected to Ag retrieval in citrate buffer solution (0.01 M), and then blocked with endogenous peroxidase blocking solution for 15 min. Afterward, the sections were probed with the primary antibodies, including anti-ASS1 (16210-1-AP, Proteintech), overnight at 4 °C. The sections were then incubated with a biotinylated streptavidin-peroxidase complex for 1 h, and the positive signals were developed and visualized using chromogen 3,3'-diaminobenzidine. The stained cells in each section were captured under a photomicroscope (Olympus, Tokyo, Japan). The staining intensity was visually scored and stratified as follows: 0 (negative), 1 (yellowish), 2 (light brown), and 3 (dark brown).

mRNA isolation and qRT-PCR in mice

Total mRNA in different tissues was extracted using a MolPure TRIeasy Plus Total RNA Kit (YEASEN, Shanghai, China) according to the manufacturer's instructions. Total RNA was reverse transcribed by a HiScript III 1st Strand cDNA Synthesis Kit (+gDNA wiper) for qPCR according to the manufacturer's instructions (Vazyme, Nanjing, China). Quantitative real-time PCR (qRT-PCR) was carried out by the Applied Biosystems QuantStudio 3 (ThermoFisher, USA) using Hieff qPCR SYBR Green Master Mix (Yeasen Biotech Co., Ltd.). The mRNA levels of the genes were calculated by normalization to the levels of GAPDH. Primer sets used were as follows: human ASS1: 5'-CTT GGGGCCAAAAGGTGTC-3' (forward), 5'-GAGGTAGCGGTCTCATCAG-3' (reverse); human ASL: 5'-CACTGGACCCATCATGGAGA-3' (forward), 5'-GGCTTTGCTGCCTGAACATC-3' (reverse); human ARG1: 5'-TCATCTGGGTGGATGCTCACAC-3' (forward), 5'-GAGAACCTGGCA CATGGAA-3' (reverse); human NOS2: 5'-GCTCTACACCTCCAATGT GACC-3' (forward), 5'-CTGCCGAGATTGAGCCTCATG-3' (reverse); human Gapdh: 5'-ACAACCTTGATCGTCCAAGG-3' (forward), 5'-GCC ATCACGCCACAGTTTC-3' (reverse); mouse Arg1: 5'-CTCCAAGCCA AAGTCCTTAGAG-3' (forward), 5'-GGAGCTGTCATTAGGGACATCA-3' (reverse); mouse Nos2: 5'-GTTCTCAGCCAACAATACAAGA-3' (forward), 5'-GTGGACGGGTCGATGTCAC-3' (reverse); mouse β-actin: 5'-CTGTGCCCATCTACGAGGGCTAT-3' (forward), 5'-TTGATGTCACGC ACGATTTC-3' (reverse).

ELISA assay

Colon tissues were accurately weighed, and 5-fold PBS containing 1% PMSF was added and homogenized for 5 min. The supernatant was collected by centrifuging at 12000 rpm for 10 min. Several ELISA kits for the determination of pro-inflammatory cytokines in serum and colon tissue homogenate of each mouse were used as follows: IL-1β (70-EK101BHS-96, MultiSciences), IL-6 (70-EK206HS-96, MultiSciences), MPO (EK2133/2-96, MultiSciences), nitric oxide (NO, S0021S, Beyotime), and Urea (E-BC-K183-M, Elabscience). For colon tissues, cytokines were normalized to the total protein content of the tissue lysate, which was determined using a BCA assay (70-PQ0012, MultiSciences).

Untargeted serum-based metabolomics

Sample preparation. An aliquot of 200 µL of methanol/acetonitrile (1:1) solution at –20 °C was added to 50 µL serum. The mixture was centrifuged at a speed of 14,000 rpm at 4 °C for 10 min to remove the precipitated protein. After that, the supernatant was collected and dried with nitrogen, and the lyophilized powder was stored at –80 °C prior to further analysis. The lyophilized samples were reconstituted by dissolving in 50 µL of the solvent mixture containing water/acetonitrile (1:1, v/v) for ultra-performance liquid chromatography with quadrupole time-of-flight mass spectrometry (UPLC-Q/TOF-MS) analysis. To monitor the stability and repeatability of instrument analysis,

quality control (QC) samples were prepared by pooling 10 μ L aliquots of each sample and pretreated using the same procedure.

UPLC-Q/TOF-MS analysis. Metabolic profiling of serum samples was performed on an Agilent 1290 Infinity system (Agilent Technologies, Santa-Clara, California, USA) coupled to an AB SCIEX Triple TOF 6600 System (AB SCIEX, Framingham, MA, USA) with an electrospray ion (ESI) source in both positive and negative ion modes. A 2 μ L aliquot of supernatant was injected into the system, and the separation was conducted on a 2.1×100 mm ACQUITY UPLC 1.7 μ m BEH HILIC column maintained at 25 °C. Ultra-pure water containing 0.1% formic acid and acetonitrile containing 0.1% formic acid were used as mobile phases A and B. Ultra-pure water containing 25 mM ammonium acetate and 25 mM ammonium hydroxide (A) and acetonitrile (B) constituted the mobile phase system. Gradient program of elution both for the ESI+ and ESI- modes was as follows: 95-95% B at 0-1 min, 95-65% B at 1-14 min, 65-40% B at 14-16 min, 40-40% B at 16-18 min, 40-95% B at 18-18.1 min, 95-95% B at 18.1-23 min. The flow rate was set at 0.3 mL/min. The Triple TOF parameters used were as follows: ion source gas 1, 60, ion source gas 2, 60; curtain gas, 30; source temperature, 600 °C; ionsapary voltage floating, 5000 V (+) and -4500 V (-); TOF MS scan m/z range, 60-1000 Da, product ion scan m/z range, 25-1000 Da; Information-dependent acquisition (IDA), an artificial intelligence-based product ion scan; declustering potential, 60 V (+) and -60 V (-); collision energy, 50 V (+) and -20 V (-); exclude isotopes within 4 Da; candidate ions to monitor per cycle, 6.

Data processing. The raw MS data (wiff.scan files) were converted to mzXML files using ProteoWizard MSConvert before inputting into the XCMS software. For peak picking, centWave m/z was set at 25 ppm, peakwidth was c (10, 60), and prefilter was c (10, 100). For peak grouping, bw was 5, mzwid was 0.025, and minfrac was 0.5. The collection of Algorithms of Metabolite pRofile Annotation was used to annotate isotopes and adducts. In the extracted ion features, only the variables with more than 50% of the nonzero measured values in at least one group were retained. Metabolite identification was performed by comparison of accurate m/z values (< 25 ppm) and MS/MS data with an in-house database with available authentic standards established by Shanghai Applied Protein Technology Co., Ltd.

After normalization of total peak intensity, the data was imported into SIMCA-P (version 14.1, Umetrics, Umea, Sweden), where multivariate data analysis was performed by Pareto-scaled principal component analysis (PCA) and partial least-squares discriminant analysis (PLS-DA) models. The PLS-DA model was seven-fold cross-validated and evaluated by the R_{2Y} and Q₂ values, in which R_{2Y} shows the interpretation rate of the model, and Q₂ indicates the prediction rate. Higher values of R_{2Y} and Q₂ indicate that the model is reliable and highly predictive. The overfitting test of the model was evaluated by a 200-permutation test. Benjamini-Hochberg false discovery rate (FDR) was employed for multiple test adjustments. The significance of each metabolite was analyzed using the Student's *t* test at a univariate level with false discovery rate (FDR) correction. Adjusted p-values less than 0.05 are considered statistically significant. Differential metabolites were screened as those with variable importance in the projection (VIP) > 1.0 obtained from PLS-DA and adjusted p-values less than 0.05, where VIP indicates the contribution of each variable to group differences. Heatmaps were obtained based on Spearman correlation and cluster analyses. Pathway analyses were measured by tidyMass⁸² and massdatabase⁸³.

Chromatin immunoprecipitation (ChIP). 100 μ g formaldehyde cross-linked nuclear proteins were precipitated with anti-BRG1 (Abcam, ab110641), anti-acetyl H3 (Millipore, 06-599), anti-trimethyl H3K4 (Millipore, 07-473), anti-dimethyl H3K9 (Millipore, 07-441), anti-trimethyl H3K9 (Abcam, Ab8898), anti-trimethyl H3K27 (Abcam,

Ab192985). Precipitated genomic DNA was amplified by real-time PCR with the following primers: ASS1 promoter, 5'-CTGATTGGACCGTG-GATGGA -3' and 5'-GCCTGTGTTACATGTCCTCAC -3'; ASS1 intron, 5'-cagggtggctgtgaacgt -3' and 5'-ggtgcccatcccagggtata -3'.

Protein extraction, immunoprecipitation, and western blot. Whole-cell lysates were obtained by re-suspending cell pellets in RIPA buffer (50 mM Tris pH 7.4, 150 mM NaCl, 1% Triton X-100). Specific antibodies or pre-immune IgGs (P.I.I.) were added to and incubated with cell lysates overnight before being absorbed by Protein A/G-plus Agarose beads (Santa Cruz). The precipitated immune complex was released by boiling with 1X SDS electrophoresis sample buffer. Western blot analyses were performed with the indicated antibodies. All experiments were repeated three times.

Targeted serum- and tissue-based metabolomics

Sample preparations. An aliquot of 150 μ L of methanol solution containing 5 μ g/mL of isotope-labeled internal standard (¹³C6 L-arginine) was added to 50 μ L serum. The mixture was centrifuged at a speed of 13,000 rpm at 4 °C for 10 min to remove the precipitated protein. After that, the 150 μ L of supernatant was collected and dried with nitrogen. Lyophilized samples were reconstituted by dissolving in 100 μ L of the solvent mixture containing water/acetonitrile (1:1, v/v) for ultra-performance liquid chromatography with triple quadrupole mass spectrometry (UPLC-QQQ/MS) analysis. Colon tissues were thawed, cut into pieces, and homogenized for 10 min with 75% methanol (1:20, w/v) containing 1 μ g/mL of ¹³C6 L-arginine using a high-speed homogenizer. The homogenate was obtained by centrifuging at 13,000 rpm for 10 min. The 120 μ L of supernatant was collected and dried with nitrogen. To monitor the stability and repeatability of instrument analysis, quality control (QC) samples were prepared by pooling 10 μ L of each sample, pretreated using the same procedure, and analyzed five times at the beginning of the run and injected once after every 30 injections of the random sequenced samples.

UPLC-QQQ/MS analysis. Targeted metabolomics was performed on a Nexera X2 UHPLC System coupled to an LCMS-8050 Triple Quadrupole Liquid Chromatograph Mass Spectrometer (LC-MS/MS) (Shimadzu, Kyoto, Japan) with an electrospray ion (ESI) source in the positive ion mode. A 1 μ L aliquot of supernatant was injected into the system, and the separation was conducted on a 2.1×100 mm ACQUITY UPLC 1.7 μ m BEH Amide column maintained at 40 °C. Ultra-pure water containing 0.2% formic acid and acetonitrile containing 0.2% formic acid were used as mobile phases A and B. Gradient program of elution was as follows: 87-87% B at 0-1 min, 87-82% B at 1-5.5 min, 82-53% B at 5.5-7.0 min, 53-50% B at 7.0-9.0 min, 50-87% B at 9.0-10.0 min, 87-87% B at 10.0-16.0 min. The flow rate was set at 0.4 mL/min. The ion source parameters were set as follows: nebulizing gas flow, 3 L/min; desolvation line temperature, 250 °C; heat block temperature, 400 °C; interface temperature, 300 °C; drying flow, 10 L/min; heating gas flow, 10 L/min. The precursor ions (m/z) for L-arginine and its isotope-labeled internal standard (¹³C6 L-arginine) were set at 175 and 181, respectively. The product ion for L-arginine was set at 70, and ¹³C6 L-arginine was 74. MS parameters were as follows: dwell time, 100 ms; Q1, -21 V; CE, -23eV; Q3, -28 V.

Label-free quantitative proteomics. Normal and inflamed colonic mucosa from UC patients were cryogenically ground with liquid nitrogen. The lysis buffer containing 0.1 M Tris-HCl (pH 7.5), 4% sodium dodecyl sulfate (SDS), and 0.1 M dithiothreitol (DTT) was added to tissue powders, and the mixture was sonicated with 20 cycles of pulses (30 s each on/off, 80% power; CosmoSonic II Ultra Sonicator). The lysates were then heated at 95 °C for 10 min and clarified by centrifugation at 16,000 $\times g$ for 20 min at room temperature. Protein concentrations were determined by measuring tryptophan

fluorescence, with excitation at 295 nm and emission at 350 nm. All experimental samples were processed in duplicate under identical conditions to ensure technical reproducibility and reliability of the experimental data. Protein (100 µg) was digested using the Filter-Aided Sample Preparation (FASP) method with 30 kDa filters (Millipore, Cat. No. MRCFOR030). Briefly, protein alkylation was performed using 50 mM iodoacetamide in the dark at room temperature for 30 min, and tryptic digestion was carried out with an enzyme-to-substrate ratio of 1:50 (w/w) at 37 °C overnight. Peptides were quantified with a peptide quantification kit (Thermo Fisher Scientific, 23275) and dissolved in 1% formic acid. For LC-MS/MS analysis, peptide samples (2 µg) were loaded onto a 25-cm column packed in-house with C₁₈ 3 µM ReproSil particles (Dr. Maisch GmbH), and analyzed with an EASY-nLC 1200 system (Thermo Fisher Scientific) coupled to the mass spectrometer (Q Exactive Plus, Thermo Fisher Scientific). The mobile phase consisted of (A) 0.1% formic acid in water and (B) 0.1% formic acid in acetonitrile/water (80:20, v/v). Column temperature was maintained at 50 °C. Peptides were separated with a 120 min gradient at a flow rate of 400 nL/min. The gradient elution program was as follows: 5% B (0–1 min), 5–32% B (1–106 min), 32–45% B (106–111 min), 45–100% B (111–113 min), and 100% B (113–120 min). MS1 scan range was set from 300 to 1700 m/z with a resolution of 70,000 (at 200 m/z), with an AGC target of 3×10^6 and a maximum injection time of 50 ms. The top 15 precursors were selected for MS/MS analysis with a resolution at 17,500 (at 200 m/z), with AGC target 1×10^5 and a maximum injection time 100 ms. The isolation window of precursors was 1.5 m/z. Normalized collision energy was set at 27 eV with a 30 s dynamic exclusion window. For quality control (QC) of the MS performance, mixed peptides from all samples were measured as a QC standard. The QC standard was run using the same method.

Raw data analysis. Raw data files were processed using the software MaxQuant (<http://www.maxquant.org>) version 2.0.3.0 with an FDR < 0.01 at the levels of proteins and peptides. The MS/MS spectra were searched against the Homo sapiens protein database in UniProt (version downloaded on November 11, 2024, comprising 83,413 protein entries). Minimum peptide length was set as 7. The mass tolerances were 20 ppm for precursor and 0.5 Da for product ions. A maximum of two missed cleavages were allowed. Protein N-terminal acetylation and oxidation of methionine were set as variable modifications, and cysteine carbamidomethylation as a fixed modification. The minimum ratio count of label-free quantification was set to 1. Bioinformatics analyses were done with R version 4.4.2 (<https://www.r-project.org/>) statistical computing software. P-values were calculated with t-test statistics and adjusted for multiple testing using Benjamini & Hochberg correction.

Molecular docking. The two-dimensional (2D) chemical structures of around 1.6 million commercially available compounds in the Chem-Div library were first converted to 3D structures using the energy minimization algorithm of MOE software (MMFF94x force field). The crystal structure of ASS1 (PDB ID: 2nz2) was prepared as the target for the molecular docking, where hydrogen atoms were added, and water molecules were removed, and the partial charges were computed using the Amber99 force field. The bound co-crystal inhibitor was used as the template to define the docking-active site in the crystal structure of ASS1. The virtual screening protocol of MOE, in combination with the triangle matcher docking algorithm, was used to screen the potential active compounds. Docking scores were calculated through the dG scoring function of the MOE software. Twenty docked conformations of each ligand were retained after docking. The lowest energy conformation was selected and subjected to an energy minimization using the MMFF94X force field. Based on the lowest binding energies, the top 500 ligands were selected for further analysis. To maintain the structural diversity of

the experimentally validated compounds and identify potential hits, we have clustered the best 500 compounds according to their structural scaffolds using the RDKit package (<https://www.rdkit.org>). We generated the Morgan fingerprints⁸⁴, which are also known as the extended-connectivity fingerprint (ECFP), of these 500 molecules based on their structures by using the RDKit AllChem. The length of the vector was set to 1024, while the radius was set to 2. Then, the Morgan fingerprints were utilized to compute the Tanimoto similarity of the dataset, where chemical fingerprint-based similarity metrics were obtained to measure the distance between pairs of molecules. Then, the Butina cluster algorithm⁸⁵ was used to make clusters, and a distance cutoff of 0.65 was used to generate 17 clusters. We evaluated the docking scores and binding modes of the molecules in each cluster (the binding position, shape complementary, formed hydrogen bonds, as well as the salt bridges), and found the representative compounds (C-01 to C-11) were selected, which were ranked at the relatively top region with favorable interactions between the selected molecules and the target. Thus, finally, we selected the compounds for experimental validation.

Molecular dynamics (MD). The MD simulation was carried out by using the Amber18 program. The Amber ff14SB force field⁸⁶ was utilized to generate the topological files for the protein via the leap module of the Amber18, while the gaff force field⁸⁷ was used for the ligand. The protein-ligand system, produced from molecular docking, was solvated in a cubic box of SPC water molecules⁸⁸, with the closest distance from the box's surface to the solute atoms set to 6 Å. The counterions (Na⁺ or Cl⁻) were added to neutralize the system. The particle mesh Ewald (PME) was employed to treat the long-range electrostatic interactions⁸⁹. The energy minimization was done in two steps. In the first step, only the solvent molecules were optimized while the solute was constrained, and the entire system was energy-minimized in the second step. Then, the system was heated gradually from 0 K to 300 K using Langevin dynamics⁹⁰ in 0.3 ns with a time step of 1 fs, with the heavy atoms of the solute constrained with a 10.0 kcal/(mol·Å²) restraint. The isothermal isobaric simulations were run 1 ns at 300 K and 1 bar to equilibrate the system fully, and then the productions were run 100 ns under the isothermal isovolumetric simulations with a time step of 2 fs. The MD simulation was repeated three times for C-01. The trajectory data was analyzed using the cpptraj module of Amber18⁹¹. The binding free energy of the ligand was calculated using the MM-GB/PBSA algorithm based on the snapshots extracted from the trajectory of the equilibrium stage with an interval of 50 ps, and the binding free energy was decomposed on per residue of ASS1, both of which were conducted with the Amber package. An initial coordinate and simulation input file, and a coordinate file of the final output has been provided as Supplementary Data 1.

Surface plasmon resonance (SPR) analysis. The interaction between C-01 and ASS1 was detected by SPR using the Biacore T200 system (GE Healthcare, USA) at 25 °C. Briefly, recombinant human ASS1 protein (Shanghai Zeye Biotechnology Co., Ltd, ZY63814HuP) was immobilized on the sensor chip (CM5, GE Healthcare) using the amine-coupling method according to standard protocols. Gradient concentrations of C-01 were injected at a flow rate of 30 µL/min in running buffer [5% (v/v) DMSO in PBS]. The SPR analysis was performed on a Biacore TM T200 instrument according to the manufacturer's instructions. The affinity fitting was carried out with Biacore T200 evaluation software by global fitting using a steady-state affinity model to obtain the affinity constant K_D .

Pharmacokinetics for C-01. After adapting for a week, male Sprague-Dawley rats (~220 g) from Shanghai SLAC Laboratory Animal CO., LTD. were fasted, but with free access to water for 12 h before conducting the pharmacokinetic experiment. The rats were orally administration

of C-01 (10 mg/kg). After dosing for 5, 15, 30, 45, 60, 90, 120, 240, 360, 480, 600, 720, and 1440 min, approximately 300 μ L blood was collected from the orbital plexus and put into heparinized 1.5 mL polythene tubes at predetermined time points. Plasma samples were prepared by centrifugation at 1816 g for 7 min. For the colonic distribution study, the 50 male ICR mice (~22 g) from Shanghai SLAC Laboratory Animal CO., LTD. were randomly divided into 10 groups ($n = 6$). All mice received a single oral administration of C-01 at a dosage of 10 mg/kg. The colon tissue was harvested after the mice were sacrificed (one sampling per mouse). All plasma and tissue samples were immediately analyzed or stored at -70 °C for further analysis. *For sample preparation*, a 50 μ L aliquot of plasma was vortex mixed with 160 μ L MeOH containing chloramphenicol (8.4 ng). The sample was vortexed for 1.5 min, and centrifuged at 9659 \times g for 10 min. The 175 μ L of supernatant was transferred into another Eppendorf tube and dried under a flow of nitrogen gas. The residue was re-constituted in 70 μ L MeOH and vortexed for 5 min, then centrifuged (9659 \times g for 10 min). The supernatant was transferred to an autosampler vial. *For the LC-MS condition*. The pharmacokinetics for C-01 was performed on an UltiMate 3000 ultra-performance liquid chromatography system (DIONEX, Sunnyvale, CA, USA) coupled to a TSQ VantageTM triple quadrupole mass spectrometer (Thermo Fisher Scientific Inc.) with an electrospray ion (ESI) source in negative ion mode. A 1 μ L aliquot of supernatant was spiked into the system, and the separation was conducted on a 2.1 \times 100 mm ACQUITY UPLC 1.7 μ m BEH C₁₈ column maintained at 40 °C. Ultra-pure water containing 0.1% formic acid and acetonitrile containing 0.1% formic acid were used as mobile phases A and B. Gradient program of elution was as follows: 30–90% B at 0–5 min, 90–30% B at 5–5.5 min, 30–30% B at 5.5–9.0 min. The flow rate was set at 0.3 mL/min. The ion source parameters were set as follows: spray voltage, 3.5 kV; vaporizer temperature, 400 °C; sheath gas pressure, 45 arb; aux gas pressure, 25 arb; capillary temperature, 320 °C. The precursor ion (m/z) for C-01 and internal standard (chloramphenicol) were set at 459.2 and 321.0, respectively. The product ion for C-01 was set to 359.2, and chloramphenicol was 151.0. The S-lens for C-01 and the internal standard were set at 85 and 80 V, respectively. The collision energy for C-01 and internal standard were set at 19 eV and 22 eV, respectively. The pharmacokinetic parameters, including the peak plasma concentration (C_{max}), the time to C_{max} (T_{max}), the AUC from 0 to infinity ($AUC_{0-\infty}$), the AUC from 0 to time (AUC_{0-t}), the mean residence time (MRT), and the terminal elimination half-life ($T_{1/2}$) were calculated by the non-compartmental analysis of plasma concentration *vs.* time data using the "DAS 2.0" software (Mathematical Pharmacology Professional Committee of China, Shanghai, China). *Single Oral Dose Toxicity Study*. ICR mice from Shanghai SLAC Laboratory Animal Co., Ltd. were acclimatized and fed on a diet of pellets and tap water ad libitum. Animals were randomly assigned to treatment groups ($n = 6$; 3 males and 3 females), acclimatized for five days, and fasted for 2 h prior to treatment administration. Mice were given a single dose by oral gavage of 100, 200 mg/kg and 400 mg/kg. Control groups received the same volume of vehicle only. Following administration, mice were clinically examined several times a day during the first day and daily thereafter for up to 14 days. All mice were euthanized at the end of the study and exsanguinated through the abdominal aorta. Complete gross postmortem examination was performed on all mice.

Organoid culture. Patient-derived colorectal normal organoids (CNOs) were recovered from cryopreserved organoid lines. The organoids were resuspended in Matrigel, seeded, and cultured in 6-well plates using the Human Colonic Organoid Kit. The culture medium was refreshed every 48 h. CNOs were passaged every 3–5 days by mechanical dissociation using a pipette tip, or with 1–2 mL of TrypLE™ Express (GIBCO, USA) when necessary.

Organoids viability assay. CNOs were digested and seeded in 96-well plates. After 24 h, different drug concentrations were applied to each group of CNOs, with the medium serving as a control. Then, TNF- α and IFN- γ were dissolved in the medium and applied to each group except the control group. Cell viability was assessed 24 h post-treatment using the CellTiter-Glo® Luminescent Cell Viability Assay (CTG) (Promega Corporation, USA) following the manufacturer's instructions.

Statistical analysis and reproducibility. Analyses were performed with Prism Software (GraphPad Software 9.0) and R version 4.2.1.

Reporting summary

Further information on research design is available in the Nature Portfolio Reporting Summary linked to this article.

Data availability

The mass spectrometry proteomics data generated in this study have been deposited in the ProteomeXchange Consortium under accession code PXD061745 via the iProX partner repository^{92,93} (<https://proteomecentral.proteomexchange.org/ui?search=PXD061745>). The mass spectrometry metabolomics data generated in this study have been deposited in the MetaboLights under Study ID MTBLS7438. The data of 16S rDNA bacteria gene sequencing generated in this study have been deposited in the SRA database in NCBI under accession code PRJNA1231628. Source data are provided in this paper.

Code availability

All the custom scripts developed for this study have been made openly accessible and can be found on the GitHub repository at https://github.com/jaspershen-lab/uc_project, and the: <https://doi.org/10.5281/zenodo.1572859>.

References

1. Gajendran, M. et al. A comprehensive review and update on ulcerative colitis. *Dis. Mon.* **65**, 100851 (2019).
2. Ungaro, R., Mehandru, S., Allen, P. B., Peyrin-Biroulet, L. & Colombel, J.-F. Ulcerative colitis. *Lancet Lond. Engl.* **389**, 1756–1770 (2017).
3. Ng, S. C. et al. Worldwide incidence and prevalence of inflammatory bowel disease in the 21st century: a systematic review of population-based studies. *Lancet* **390**, 2769–2778 (2017).
4. Kaser, A., Zeissig, S. & Blumberg, R. S. Inflammatory bowel disease. *Annu. Rev. Immunol.* **28**, 573–621 (2010).
5. Nishida, A. et al. Gut microbiota in the pathogenesis of inflammatory bowel disease. *Clin. J. Gastroenterol.* **11**, 1–10 (2017).
6. Tang, X. et al. Butyric acid increases the therapeutic effect of EHLJ7 on ulcerative colitis by inhibiting JAK2/STAT3/SOCS1 Signaling Pathway. *Front. Pharmacol.* **10**, 1553 (2020).
7. Jørgensen, J. & Mortensen, P. B. Substrate utilization by intestinal mucosal tissue strips from patients with inflammatory bowel disease. *Am. J. Physiol. Gastrointest. Liver Physiol.* **281**, G405–G411 (2001).
8. Harbord, M. et al. Third European evidence-based consensus on diagnosis and management of ulcerative colitis. Part 2: Current management. *J. Crohns Colitis* **11**, 769–784 (2017).
9. Rubin, D. T., Ananthakrishnan, A. N., Siegel, C. A., Sauer, B. G. & Long, M. D. ACG Clinical guideline: Ulcerative colitis in adults. *Am. J. Gastroenterol.* **114**, 384–413 (2019).
10. Kobayashi, T. et al. Ulcerative colitis. *Nat. Rev. Dis. Prim.* **6**, 74 (2020).
11. Shen, X. et al. Metabolic reaction network-based recursive metabolite annotation for untargeted metabolomics. *Nat. Commun.* **10**, 1516 (2019).
12. Zhu, G. et al. The application of omics techniques to evaluate the effects of Tanshinone IIA on dextran sodium sulfate induced ulcerative colitis. *Mol. Omics* **18**, 666–676 (2022).

13. Kolho, K.-L., Pessia, A., Jaakkola, T., de Vos, W. M. & Velagapudi, V. Faecal and serum metabolomics in paediatric inflammatory bowel disease. *J. Crohns Colitis* **11**, jjw158 (2016).
14. Diab, J. et al. Lipidomics in ulcerative colitis reveal alteration in mucosal lipid composition associated with the disease state. *Inflamm. Bowel Dis.* **25**, 1780–1787 (2019).
15. Liao, Z. et al. LC-MS-based metabolomics analysis of Berberine treatment in ulcerative colitis rats. *J. Chromatogr. B* **1133**, 121848 (2019).
16. Probert, F. et al. Plasma nuclear magnetic resonance metabolomics discriminates between high and low endoscopic activity and predicts progression in a prospective cohort of patients with ulcerative colitis. *J. Crohns Colitis* **12**, 1326–1337 (2018).
17. Rees, N. P. et al. Systematic review of donor and recipient predictive biomarkers of response to faecal microbiota transplantation in patients with ulcerative colitis. *eBioMedicine* **81**, 104088 (2022).
18. Iyer, S. S. et al. Dietary and microbial oxazoles induce intestinal inflammation by modulating aryl hydrocarbon receptor responses. *Cell* **173**, 1123–1134.e11 (2018).
19. Wang, C. et al. Microbial metabolite deoxycholic acid-mediated ferroptosis exacerbates high-fat diet-induced colonic inflammation. *Mol. Metab.* **84**, 101944 (2024).
20. Li, D. et al. Gut microbial metabolite deoxycholic acid facilitates Th17 differentiation through modulating cholesterol biosynthesis and participates in high-fat diet-associated colonic inflammation. *Cell Biosci.* **13**, 186 (2023).
21. Michaudel, C. et al. Rewiring the altered tryptophan metabolism as a novel therapeutic strategy in inflammatory bowel diseases. *Gut* **72**, 1296–1307 (2022).
22. Zhou, C. et al. SCFAs induce autophagy in intestinal epithelial cells and relieve colitis by stabilizing HIF-1 α . *J. Mol. Med.* **98**, 1189–1202 (2020).
23. Wu, M.-M. et al. Dioscin ameliorates murine ulcerative colitis by regulating macrophage polarization. *Pharmacol. Res.* **172**, 105796 (2021).
24. Chen, C.-L., Hsu, S.-C., Ann, D. K., Yen, Y. & Kung, H.-J. Arginine signaling and cancer metabolism. *Cancers* **13**, 3541 (2021).
25. Zhou, M. et al. Boosting mTOR-dependent autophagy via upstream TLR4-MyD88-MAPK signalling and downstream NF- κ B pathway quenches intestinal inflammation and oxidative stress injury. *eBioMedicine* **35**, 345–360 (2018).
26. Maaten, L. vander & Hinton, G. Visualizing data using t-SNE. *J. Mach. Learn. Res* **9**, 2579–2605 (2008).
27. Du, T. & Han, J. Arginine metabolism and its potential in treatment of colorectal cancer. *Front. Cell Dev. Biol.* **9**, 658861 (2021).
28. Keshet, R. & Erez, A. Arginine and the metabolic regulation of nitric oxide synthesis in cancer. *Dis. Model. Mech.* **11**, dmm033332 (2018).
29. Sarkar, D. & Sau, A. K. Illuminating the structure-function landscape of an evolutionary nonconserved motif in the arginases of Helicobacter gastric pathogens. *IUBMB Life* **75**, 782–793 (2023).
30. Lashgari, N.-A. et al. Targeting mammalian target of rapamycin: Prospects for the treatment of inflammatory bowel diseases. *Curr. Med. Chem.* **28**, 1605–1624 (2021).
31. Shen, L.-J., Belousov, K. & Shen, W.-C. Accessibility of endothelial and inducible nitric oxide synthase to the intracellular citrulline-arginine regeneration pathway. *Biochem. Pharmacol.* **69**, 97–104 (2005).
32. Keshet, R. et al. Targeting purine synthesis in ASS1-expressing tumors enhances the response to immune checkpoint inhibitors. *Nat. Cancer* **1**, 894–908 (2020).
33. Hayashi, D. et al. Valproic acid up-regulates the whole NO-citrulline cycle for potent iNOS-NO signaling to promote neuronal differentiation of adipose tissue-derived stem cells. *Nitric Oxide* **106**, 35–44 (2021).
34. Hong, Z.-S. et al. Moringa oleifera Lam. peptide remodels intestinal mucosal barrier by inhibiting JAK-STAT activation and modulating gut microbiota in colitis. *Front. Immunol.* **13**, 924178 (2022).
35. Wilson, A. et al. Trimethylamine-N-oxide: A novel biomarker for the identification of inflammatory bowel disease. *Dig. Dis. Sci.* **60**, 3620–3630 (2015).
36. Huang, K. & Fingar, D. C. Growing knowledge of the mTOR signaling network. *Semin. Cell Dev. Biol.* **36**, 79–90 (2014).
37. Laplante, M. & Sabatini, D. M. mTOR signaling in growth control and disease. *Cell* **149**, 274–293 (2012).
38. Hu, S. et al. mTOR Inhibition attenuates dextran sulfate sodium-induced colitis by suppressing T cell proliferation and balancing TH1/TH17/Treg profile. *PLOS ONE* **11**, e0154564 (2016).
39. Cosin-Roger, J. et al. Hypoxia ameliorates intestinal inflammation through NLRP3/mTOR downregulation and autophagy activation. *Nat. Commun.* **8**, 98 (2017).
40. Farkas, S. et al. Rapamycin decreases leukocyte migration in vivo and effectively reduces experimentally induced chronic colitis. *Int. J. Colorectal Dis.* **21**, 747–753 (2005).
41. Matsuda, C. et al. Therapeutic effect of a new immunosuppressive agent, everolimus, on interleukin-10 gene-deficient mice with colitis. *Clin. Exp. Immunol.* **148**, 348–359 (2007).
42. Ren, W. et al. mTORC1 signaling and IL-17 expression: Defining pathways and possible therapeutic targets. *Eur. J. Immunol.* **46**, 291–299 (2015).
43. Noviello, D. et al. The IL23-IL17 Immune axis in the treatment of ulcerative colitis: Successes, defeats, and ongoing challenges. *Front. Immunol.* **12**, 611256 (2021).
44. Lin, X. et al. Colonic epithelial mTORC1 promotes ulcerative colitis through COX-2-mediated Th17 responses. *Mucosal Immunol.* **11**, 1663–1673 (2018).
45. Wu, X. et al. Arctigenin exerts anti-colitis efficacy through inhibiting the differentiation of Th1 and Th17 cells via an mTORC1-dependent pathway. *Biochem. Pharmacol.* **96**, 323–336 (2015).
46. Guan, Y. et al. Repression of mammalian target of rapamycin complex 1 inhibits intestinal regeneration in acute inflammatory bowel disease models. *J. Immunol.* **195**, 339–346 (2015).
47. Ren, W. et al. Dietary arginine supplementation of mice alters the microbial population and activates intestinal innate immunity. *J. Nutr.* **144**, 988–995 (2014).
48. Flam, B. R., Eichler, D. C. & Solomonson, L. P. Endothelial nitric oxide production is tightly coupled to the citrulline-NO cycle. *Nitric Oxide* **17**, 115–121 (2007).
49. Husson, A., Brasse-Lagnel, C., Fairand, A., Renouf, S. & Lavoinne, A. Argininosuccinate synthetase from the urea cycle to the citrulline-NO cycle. *Eur. J. Biochem.* **270**, 1887–1899 (2003).
50. Meng, Y. et al. The NCF1 variant p.R90H aggravates autoimmunity by facilitating the activation of plasmacytoid dendritic cells. *J. Clin. Invest.* **132**, e153619 (2022).
51. Xue, G., Hua, L., Zhou, N. & Li, J. Characteristics of immune cell infiltration and associated diagnostic biomarkers in ulcerative colitis: results from bioinformatics analysis. *Bioengineered* **12**, 252–265 (2021).
52. Long, Y. et al. Arginine deiminase resistance in melanoma cells is associated with metabolic reprogramming, glucose dependence, and glutamine addiction. *Mol. Cancer Ther.* **12**, 2581–2590 (2013).
53. Li, Y.-Y. et al. BRAF inhibitor resistance enhances vulnerability to arginine deprivation in melanoma. *Oncotarget* **7**, 17665–17680 (2016).
54. Tsai, W.-B. et al. Chromatin remodeling system p300-HDAC2-Sin3A is involved in Arginine Starvation-Induced HIF-1 α Degradation at the ASS1 promoter for ASS1 Derepression. *Sci. Rep.* **7**, 10814 (2017).
55. Wang, H.-Y. et al. Histone demethylase KDM3A is required for enhancer activation of hippo target genes in colorectal cancer. *Nucleic Acids Res.* **47**, 2349–2364 (2019).

56. Wang, Z. et al. Acetylation of PHF5A modulates stress responses and colorectal carcinogenesis through alternative splicing-mediated upregulation of KDM3A. *Mol. Cell* **74**, 1250–1263.e6 (2019).
57. Baier, J. et al. Arginase impedes the resolution of colitis by altering the microbiome and metabolome. *J. Clin. Invest.* **130**, 5703–5720 (2020).
58. Akazawa, Y. et al. Inhibition of arginase ameliorates experimental ulcerative colitis in mice. *Free Radic. Res.* **47**, 137–145 (2013).
59. Stettner, N. et al. Induction of Nitric-Oxide Metabolism in Enterocytes Alleviates Colitis and Inflammation-Associated Colon Cancer. *Cell Rep.* **23**, 1962–1976 (2018).
60. Tarasenko, T. N., Gomez-Rodriguez, J. & McGuire, P. J. Impaired T cell function in argininosuccinate synthetase deficiency. *J. Leukoc. Biol.* **97**, 273–278 (2014).
61. Lercher, A. et al. Type I interferon signaling disrupts the hepatic urea cycle and alters systemic metabolism to suppress T cell function. *Immunity* **51**, 1074–1087.e9 (2019).
62. Mao, Y., Shi, D., Li, G. & Jiang, P. Citrulline depletion by ASS1 is required for proinflammatory macrophage activation and immune responses. *Mol. Cell* **82**, 527–541 (2022).
63. Hong, S.-K. S. et al. Increased serum levels of L-arginine in ulcerative colitis and correlation with disease severity. *Inflamm. Bowel Dis.* **16**, 105–111 (2010).
64. Krzystek-Korpacka, M. et al. Transcriptional and metabolomic analysis of L-arginine/nitric oxide pathway in inflammatory bowel disease and its association with local inflammatory and angiogenic response: Preliminary findings. *Int. J. Mol. Sci.* **21**, 1641 (2020).
65. Coburn, L. A. et al. L-arginine supplementation improves responses to injury and inflammation in dextran sulfate sodium colitis. *PLoS ONE* **7**, e33546 (2012).
66. Coburn, L. A. et al. L-Arginine availability and metabolism is altered in ulcerative colitis. *Inflamm. Bowel Dis.* **22**, 1847–1858 (2016).
67. Li, J.-Y. et al. Arginine metabolism regulates the pathogenesis of inflammatory bowel disease. *Nutr. Rev.* **81**, 578–586 (2022).
68. Singh, K. et al. Dietary arginine regulates severity of experimental colitis and affects the colonic microbiome. *Front. Cell. Infect. Microbiol.* **9**, 66 (2019).
69. Andrade, M. E. R. et al. Pretreatment and treatment with L-arginine attenuate weight loss and bacterial translocation in dextran sulfate sodium colitis. *J. Parenter. Enter. Nutr.* **40**, 1131–1139 (2015).
70. Ren, W. et al. Serum amino acids profile and the beneficial effects of L-arginine or L-glutamine supplementation in dextran sulfate sodium colitis. *PLoS ONE* **9**, e88335 (2014).
71. Perner, A. et al. Expression of nitric oxide synthases and effects of L-arginine and L-NMMA on nitric oxide production and fluid transport in collagenous colitis. *Gut* **49**, 387–394 (2001).
72. Missiaen, R. et al. GCN2 inhibition sensitizes arginine-deprived hepatocellular carcinoma cells to senolytic treatment. *Cell Metab.* **34**, 1151–1167 (2022).
73. Sun, N. & Zhao, X. Argininosuccinate synthase 1, arginine deprivation therapy and cancer management. *Front. Pharmacol.* **13**, 935553 (2022).
74. Nüse, B., Holland, T., Rauh, M., Gerlach, R. G. & Mattner, J. L-arginine metabolism as pivotal interface of mutual host-microbe interactions in the gut. *Gut Microbes* **15**, 2222961 (2023).
75. Szefel, J., Danielak, A. & Kruszewski, W. J. Metabolic pathways of L-arginine and therapeutic consequences in tumors. *Adv. Med. Sci.* **64**, 104–110 (2019).
76. Dong, J., Wu, B. & Tian, W. Human adipose tissue-derived small extracellular vesicles promote soft tissue repair through modulating M1-to-M2 polarization of macrophages. *Stem Cell Res. Ther.* **14**, 67 (2023).
77. Wang, D., Tai, P. W. L. & Gao, G. Adeno-associated virus vector as a platform for gene therapy delivery. *Nat. Rev. Drug Discov.* **18**, 358–378 (2019).
78. Moniruzzaman, M. et al. IL-20 Activates ERK1/2 and Suppresses Splicing of X-Box Protein-1 in Intestinal Epithelial Cells but Does Not Improve Pathology in Acute or Chronic Models of Colitis. *Int. J. Mol. Sci.* **24**, 174 (2022).
79. Zhang, Q. et al. GPR84 signaling promotes intestinal mucosal inflammation via enhancing NLRP3 inflammasome activation in macrophages. *Acta Pharmacol. Sin.* **43**, 2042–2054 (2021).
80. Miyoshi, H. & Stappenbeck, T. S. In vitro expansion and genetic modification of gastrointestinal stem cells in spheroid culture. *Nat. Protoc.* **8**, 2471–2482 (2013).
81. Giacomin, P., Agha, Z. & Loukas, A. Helminths and Intestinal Flora Team Up to Improve Gut Health. *Trends Parasitol.* **32**, 664–666 (2016).
82. Shen, X. et al. TidyMass an object-oriented reproducible analysis framework for LC-MS data. *Nat. Commun.* **13**, 4365 (2022).
83. Shen, X., Wang, C. & Snyder, M. P. massDatabase: utilities for the operation of the public compound and pathway database. *Bioinformatics* **38**, 4650–4651 (2022).
84. Downing, J. et al. SPECTRa-T: machine-based data extraction and semantic searching of chemistry e-theses. *J. Chem. Inf. Model.* **50**, 251–261 (2010).
85. Platts, J. A., Abraham, M. H., Butina, D. & Hersey, A. Estimation of molecular linear free energy relationship descriptors by a group contribution approach. 2. Prediction of partition coefficients. *J. Chem. Inf. Comput. Sci.* **40**, 71–80 (1999).
86. Maier, J. A. et al. ff14SB: Improving the Accuracy of Protein Side Chain and Backbone Parameters from ff99SB. *J. Chem. Theory Comput.* **11**, 3696–3713 (2015).
87. Wang, J., Wolf, R. M., Caldwell, J. W., Kollman, P. A. & Case, D. A. Development and testing of a general amber force field. *J. Comput. Chem.* **25**, 1157–1174 (2004).
88. Alejandre, J., Chapela, G. A., Bresme, F. & Hansen, J.-P. The short range anion-H interaction is the driving force for crystal formation of ions in water. *J. Chem. Phys.* **130**, 174505 (2009).
89. Simonett, A. C. & Brooks, B. R. A compression strategy for particle mesh Ewald theory. *J. Chem. Phys.* **154**, 054112 (2021).
90. Berti, C. et al. Three-dimensional brownian dynamics simulator for the study of ion permeation through membrane pores. *J. Chem. Theory Comput.* **10**, 2911–2926 (2014).
91. Roe, D. R. & Cheatham, T. E. PTRAJ and CPPTRAJ: Software for processing and analysis of molecular dynamics trajectory data. *J. Chem. Theory Comput.* **9**, 3084–3095 (2013).
92. Ma, J. et al. iProX: an integrated proteome resource. *Nucleic Acids Res.* **47**, D1211–D1217 (2018).
93. Chen, T. et al. iProX in 2021: connecting proteomics data sharing with big data. *Nucleic Acids Res.* **50**, D1522–D1527 (2021).

Acknowledgements

This work was financially supported by the National Natural Science Foundation of China (Grant 82074241 and 82474265 to S.J.L., 82274071 to W.Z.), the Special Project of Life and Health Science and Technology of Nanjing Science and Technology Bureau (Grant 202110024 to S.J.L.), the Project of Jiangsu Province Hospital of Traditional Chinese Medicine Peak Talent (Grant y2021rc36 to S.J.L.), high-level introduction of talents and scientific research start-up funds of CPU (Grant 3150020068 to H.J.S.), high-level introduction of talents and scientific research start-up funds of JNU (Grant 1286010241222100 to H.J.S.). Z.J.D. and X.T.S. were supported by the start-up package from Lee Kong Chian School of Medicine, School of Chemistry, Chemical Engineering and Biotechnology, NTU (X.T.S.). We thank Aifeng Zhang from Southeast University for hematoxylin-eosin staining and immunohistochemistry scores. We thank Jing Sun from the Department of Gastroenterology, Wuxi People's Hospital Affiliated to Nanjing Medical University for manuscript revisions. We thank Haidan Wang from the Affiliated Hospital of Nanjing University of Chinese Medicine for animal experiments.

Author contributions

W.Z., X.T.S., H.J.S., S.J.L., and G.C. designed the research, wrote, and reviewed the manuscript. S.J.L. collected clinical samples and performed omics analysis. Z.J.D., S.L., Y.Z., Z.C.L., L.W., Z.M.F., P.W., Y.J.Y., J.Z.Z., T.T.L., Q.Z.H., X.G., and S.S.Y. performed most of the experiments and implemented the data analysis. J.J.Z., H.B.H., K.D., and Y.X. collected clinical samples. C.L.Y. helped to perform the proteomics. Z.J.D., C.W.W., W.C.X., and J.J.S. conducted the metabolomics. X.T.S. and Z.J.D. conducted the omics data analysis and did the data visualizations. Y.M.L., Z.J.D., and X.T.S. contributed to the manuscript writing and reviewing. W.Z. served as the lead contact for this work.

Competing interests

The authors declare no competing interests.

Additional information

Supplementary information The online version contains supplementary material available at
<https://doi.org/10.1038/s41467-025-62217-8>.

Correspondence and requests for materials should be addressed to Shijia Liu, Haijian Sun, Xiaotao Shen, Gang Cao or Wei Zhou.

Peer review information *Nature Communications* thanks Caroline Evans and the other anonymous reviewer(s) for their contribution to the peer review of this work. A peer review file is available.

Reprints and permissions information is available at
<http://www.nature.com/reprints>

Publisher's note Springer Nature remains neutral with regard to jurisdictional claims in published maps and institutional affiliations.

Open Access This article is licensed under a Creative Commons Attribution-NonCommercial-NoDerivatives 4.0 International License, which permits any non-commercial use, sharing, distribution and reproduction in any medium or format, as long as you give appropriate credit to the original author(s) and the source, provide a link to the Creative Commons licence, and indicate if you modified the licensed material. You do not have permission under this licence to share adapted material derived from this article or parts of it. The images or other third party material in this article are included in the article's Creative Commons licence, unless indicated otherwise in a credit line to the material. If material is not included in the article's Creative Commons licence and your intended use is not permitted by statutory regulation or exceeds the permitted use, you will need to obtain permission directly from the copyright holder. To view a copy of this licence, visit <http://creativecommons.org/licenses/by-nc-nd/4.0/>.

© The Author(s) 2025